Kalman tracking and estimation of continuous gravitational waves with a pulsar timing array: inclusion of the pulsar terms

Tom Kimpson[1,2]★, Andrew Melatos[1,2], Joseph O'Leary[1,2], Julian B. Carlin[1,2], Robin J. Evans[3], William Moran[3], Tong Cheunchitra[1,2], Wenhao Dong[1,2], Liam Dunn[1,2], Julian Greentree[3], Nicholas J. O'Neill[1,2], Sofia Suvorova[3], Kok Hong Thong[1,2], Andrés F. Vargas[1,2]

[1]*School of Physics, University of Melbourne, Parkville, VIC 3010, Australia*
[2]*OzGrav, University of Melbourne, Parkville, VIC 3010, Australia*
[3]*Department of Electrical and Electronic Engineering, University of Melbourne, Parkville, Victoria 3010, Australia*

ABSTRACT

The detection of continuous nanohertz gravitational waves from individual supermassive black hole binaries can be formulated within a state-space framework, wherein intrinsic achromatic spin wandering is tracked simultaneously with the modulation induced by a single-source gravitational wave in the pulse times of arrival. Such an approach complements traditional analysis methods by enabling self-consistent inference of model parameters and calculation of the Bayesian evidence, without fitting for ensemble-averaged statistics such as the power spectral density of the timing noise. Previous analyses have worked exclusively with the 'Earth term', leading to biases in the parameter estimation. Here it is shown how to extend previous analyses to include the so-called 'pulsar terms'. It is shown via astrophysically representative software injections in Gaussian measurement noise that the inclusion of the pulsar terms eliminates the biases in the parameter estimates, increasing the parameter accuracy relative to the Earth terms approach by X and the sensitivity by Y.

Key words: gravitational waves – methods: data analysis – pulsars: general

1 INTRODUCTION

Nanohertz gravitational waves (GWs) can be produced by the inspiral of supermassive black hole binaries (SMBHBs; Rajagopal & Romani 1995; Jaffe & Backer 2003; Wyithe & Loeb 2003; Sesana 2013; McWilliams et al. 2014; Ravi et al. 2015; Burke-Spolaor et al. 2019; Sykes et al. 2022). A nHz GW influences the times of arrival (TOAs) of radio pulses from pulsars measured at the Earth. A pulsar timing array (PTA Tiburzi 2018; Verbiest et al. 2021) simultaneously measures the TOAs from multiple pulsars. In this way it is possible to detect GWs at frequencies that are prohibitively low for terrestrial interferometers.

PTAs search for two types of SMBHB GW signals. The first is a stochastic GW background due to the incoherent superposition of multiple SMBHB sources (Allen 1997; Sesana et al. 2008; Christensen 2019; Renzini et al. 2022). Consilient evidence for the GW background has been presented by multiple separate PTAs (Agazie et al. 2023a; Antoniadis et al. 2023a; Reardon et al. 2023; Xu et al. 2023), by measuring the cross-correlation between pairs of pulsars in the pulsar timing residuals as a function of the angular separation between the pulsars – the Hellings-Downs curve (Hellings & Downs 1983). The second is resolved GWs from sufficiently close and massive individual SMBHBs (Sesana & Vecchio 2010; Yardley et al. 2010; Zhu et al. 2015a; Babak & Sesana 2012a; Ellis 2013;

Zhu et al. 2016). Individual SMBHBs are sources of continuous GWs. This results in persistent, quasi-monochromatic modulations in the pulsar timing residuals which can be modelled. Therefore, rather than cross-correlating pulsar pairs, individual SMBHBs are detected by either frequentist matched filtering (Lee et al. 2011; Ellis et al. 2012; Zhu et al. 2014) or Bayesian inference (Ellis & Cornish 2016; Arzoumanian et al. 2020a). Observational efforts to detect individual sources have been unsuccessful so far (Jenet et al. 2004; Zhu et al. 2014; Babak et al. 2016; Arzoumanian et al. 2023), although some inconclusive evidence at low significance has been presented (Antoniadis et al. 2023c).

Irregularities in the intrinsic rotation of the pulsar result in random, unmodelled, red-spectrum TOA fluctuations known as 'timing noise'. Timing noise limits the sensitivity of PTAs to GW signals (Shannon & Cordes 2010a; Lasky et al. 2015; Caballero et al. 2016; Goncharov et al. 2021). Additional white noise sources such as phase jitter noise and radiometer noise (Cordes & Shannon 2010; Lam et al. 2019; Parthasarathy et al. 2021) must also be considered. Kimpson (2023) (K23 hereafter) presented an alternative and complementary approach to PTA data analysis for individual, quasi-monochromatic, SMBHB sources which self-consistently tracks the intrinsic timing noise in PTA pulsars and disentangles it from GW-induced TOA modulations. Specifically, K23 formulate PTA analysis as a state-space problem and use a Kalman filter (Kalman 1960) to track the pulsars' intrinsic rotational state in conjunction with a Bayesian nested sampler (Skilling 2006; Ashton et al. 2022) for pa-

rameter estimation and model selection. **VALIDATION TESTS ON SYNTHETIC DATA...** newline

It is common in standard PTA analysis to drop the so called "pulsar term" from the modelling (e.g. Sesana & Vecchio 2010; Babak & Sesana 2012a; Petiteau et al. 2013; Zhu et al. 2015b; Taylor et al. 2016; Goldstein et al. 2018; Charisi et al. 2023). Unlike the "Earth term", the pulsar term is not phase coherent and cannot be summed across the array to increase the total signal-to-noise. Instead it is considered as a source of self noise. However, dropping the pulsar terms results in a reduced detection probability ($\sim 5\%$) bias in the parameter estimates (Zhu et al. 2016; Chen & Wang 2022). The method presented in K23 also drops the pulsar term. In this paper we remove this limitation and present the state-space approach to PTA data analysis including the pulsar term.

This paper is organised as follows. In Section 2 we briefly review the state-space formulation of PTA data analysis introduced in Kimpson (2023). We do not review the methods for state tracking, parameter inference and model selection and refer the reader to K23 for details. In Section 3 we introduce how to include the pulsar term in the state-space model. In Section 4 we test the updated method on the synthetic data for a single representative example GW system, and compare the results to the original Earth-terms model. In Section 8 we extend the tests to cover an astrophysically relevant parameter space. Discussion on future extensions and conclusions are made in Sections 10 and 11 respectively. Throughout the paper we adopt the natural units, with $c = G = \hbar = 1$, and metric signature $(-,+,+,+)$.

2   STATE-SPACE FORMULATION

In this section we briefly review the state-space formulation of PTA analysis presented in K23.

There are N pulsars in the array. The index n labels the n-th pulsar, with $1 \leqslant n \leqslant N$. The intrinsic spin frequency of the n-th pulsar as measured in the local, freely-falling rest frame of the pulsar's centre of mass, $f_p^{(n)}(t)$, evolves according to a stochastic differential equation. The radio pulse frequency measured by an observer at Earth, $f_m^{(n)}(t)$, is related to $f_p^{(n)}(t)$ via a measurement equation. In Section 2.1 we review the phenomenological model for the evolution of $f_p^{(n)}(t)$. In Section 2.2 we review the measurement equation which relates $f_m^{(n)}(t)$ to $f_p^{(n)}(t)$. In Section 2.3 we summarise the parameters of the model.

2.1   Spin evolution

In the model $f_p^{(n)}(t)$ evolves according to an Ornstein-Uhlenbeck process, described by a Langevin equation with a time-dependent drift term (Vargas & Melatos 2023)

$$\frac{df_p^{(n)}}{dt} = -\gamma^{(n)}[f_p^{(n)} - f_{em}^{(n)}(t)] + \dot{f}_{em}^{(n)}(t) + \xi^{(n)}(t) , \tag{1}$$

where $f_{em}^{(n)}$ is the deterministic evolution, $\dot{f}_{em}^{(n)}$ is the spin derivative, $\gamma^{(n)}$ is a damping constant whose reciprocal specifies the mean-reversion timescale, and $\xi^{(n)}(t)$ is a white noise stochastic process

which satisfies:

$$\langle \xi^{(n)}(t) \rangle = 0 , \tag{2}$$

$$\langle \xi^{(n)}(t)\xi^{(n')}(t') \rangle = [\sigma^{(n)}]^2 \delta_{n,n'}(t - t') . \tag{3}$$

In Equation (3) $[\sigma^{(n)}]^2$ is the variance of $\xi^{(n)}$ and parametrizes noise amplitude and the gives characteristic root mean square fluctuations $\approx \sigma^{(n)}/[\gamma^{(n)}]^{1/2}$ in $f_p^{(n)}(t)$ (Gardiner 2009). The deterministic evolution $f_{em}^{(n)}$ is attributed to magnetic dipole braking, with braking index $n_{em} = 3$ (Goldreich & Julian 1969). PTAs are typically composed of millisecond pulsars, for which the quadratic correction due to n_{em} in $f_p^{(n)}(t)$ is negligible over the observation time $T_{obs} \sim 10$ yr, and can be approximated accurately by

$$f_{em}^{(n)}(t) = f_{em}^{(n)}(t_1) + \dot{f}_{em}^{(n)}(t_1)t , \tag{4}$$

where an overdot denotes a derivative with respect to t and t_1 labels the time of the first TOA.

Equation 1 is inherently an idealized phenomenological model to capture the main qualitative features of a typical PTA pulsar's observed spin evolution, i.e. random, mean-reverting, small-amplitude excursions around a smooth, secular trend (Agazie et al. 2023b; Antoniadis et al. 2023b; Zic et al. 2023). Such a phenomenological model is necessary since a predictive, first-principles theory of timing noise does not currently exist c.f. the multiple theorized mechanisms of timing noise, see the discussion in Section 1 of K23. Similar approaches, analogous to Equations (4)–(3) have been followed successfully in other timing analyses in the context of anomalous braking indices (Vargas & Melatos 2023) and hidden Markov model glitch searches (Melatos et al. 2020; Lower et al. 2021; Dunn et al. 2022, 2023). However, Equation (1) does contain certain modelling omissions and idealisations which much be recognized (Meyers et al. 2021b,a; Vargas & Melatos 2023). These include: exclusion of phenomenological elements, which are likely to be present in reality, e.g. the classic, two-component, crust-superfluid structure inferred from post-glitch recoveries (Baym et al. 1969; van Eysden & Melatos 2010; Gügercinoğlu & Alpar 2017; Meyers et al. 2021a,b), the exclusion of non-Gaussian excursions such as Lévy flights (Sornette 2004), the suitability of the white noise driver $\xi(t)$ for millisecond pulsars in PTAs and the formal interpretation of $d^2 f_p/dt^2$.

2.2   Modulation of pulsar frequency by a GW

In the presence of a GW the intrinsic pulsar spin frequency for the n-th pulsar as is related to the radio pulse frequency measured by an observer on Earth as

$$f_m^{(n)}(t) = f_p^{(n)}(t - d^{(n)})g^{(n)}(t) + \varepsilon^{(n)} . \tag{5}$$

where $d^{(n)}$ labels the distance to the n-th pulsar, and $\varepsilon^{(n)}$ is a Gaussian measurement noise which satisfies:

$$\langle \varepsilon^{(n)}(t) \rangle = 0 , \tag{6}$$

$$\langle \varepsilon^{(n)}(t)\varepsilon^{(n')}(t') \rangle = \sigma_m^2 \delta_{n,n'}(t - t') . \tag{7}$$

where σ_m is the covariance of the measurement noise and is shared between all pulsars. The measurement function $g^{(n)}(t)$ is

$$g^{(n)}(t) = 1 - \frac{H_{ij}[q^{(n)}]^i[q^{(n)}]^j}{2[1 + \boldsymbol{n} \cdot \boldsymbol{q}^{(n)}]}$$
$$\times \Big[\cos(-\Omega t + \Phi_0)$$
$$- \cos\Big\{ -\Omega t + \Phi_0 + \Omega \big[1 + \boldsymbol{n} \cdot \boldsymbol{q}^{(n)} \big] d^{(n)} \Big\} \Big] . \tag{8}$$

where $[q^{(n)}]^i$ labels the i-th coordinate component of the n-th pulsar's position vector $\boldsymbol{q}^{(n)}$, $\boldsymbol{n}$ the propagation direction of the GW, Ω is the constant angular frequency of the GW, H_{ij} is the spatial part of the GW amplitude tensor and Φ_0 the phase offset of the GW.

Equation (8) contains a number of simplifying assumptions:

(i) The GW is monochromatic plane wave.
(ii) The pulsar locations are constant with respect to the observer

Regarding point (i), studies of SMBHB inspirals in the PTA context show that the gravitational wave frequency $f_{\rm gw}$ (= $\Omega/2\pi$) evolves according to (e.g. Zhu et al. 2015a),

$$\Delta f_{\rm gw} \simeq 3.94 \,\mathrm{nHz} \left(\frac{M_c}{10^9 M_\odot}\right)^{5/3} \left[\frac{f_{\rm gw}(t=t_1)}{10^{-7}\,\mathrm{Hz}}\right]^{11/3} \left(\frac{T_{\rm obs}}{10\mathrm{yr}}\right), \qquad (9)$$

where M_c is the chirp mass of the SMBHB, $f_{\rm gw}(t=t_1)$ is the GW frequency at the time of the first observation, and $T_{\rm obs}$ is the length of time over which $\Delta f_{\rm gw}$ is measured, which for PTAs is ~ 10 years. A source can be considered monochromatic, if $\Delta f_{\rm gw}$ is less than the PTA frequency resolution $1/T_{\rm obs}$. From Equation (9) we can see that only those binaries which are massive or at high frequency experience significant frequency evolution over typical PTA timespans. The majority of SMBHBs detectable with PTAs are expected to satisfy $\Delta f_{\rm gw} < 1/T_{\rm obs}$; for a PTA composed of pulsars with a mean distance of 1.5 kpc, 78% of simulated SMBHBs satisfy this condition for the current IPTA, whilst for the second phase of the Square Kilometer Array this fraction drops to 52%; see Figure 7 in Rosado et al. (2015). We are therefore justified in treating the GW source as monochromatic as a first pass in this introductory paper (Sesana et al. 2008; Sesana & Vecchio 2010; Ellis et al. 2012). Regarding point (ii) whilst in practice the pulsar locations vary with respect to the Earth, pulsar TOAs are defined relative to the Solar System barycentre (SSB). The barycentering correction is typically applied when generating TOAs, e.g. with TEMPO2 (Hobbs et al. 2006) and related timing software, and is inherited by the frequency time series. Some pulsars, including some PTA pulsars, do have non-negligible proper motions $O(100)$ km s^{-1} after the barycentering corrections have been applied (e.g. Jankowski et al. 2018), but we do not consider this effect in this paper.

2.3 Parameters of the model

The set of static parameters which determine the intrinsic frequency evolution of the pulsars in the array outlined in Section 2.1 are:

$$\boldsymbol{\theta}_{\rm psr} = \left\{\gamma^{(n)}, \sigma^{(n)}, f_{\rm em}^{(n)}(t_1), \dot{f}_{\rm em}^{(n)}(t_1), d^{(n)}\right\}_{1\leqslant n\leqslant N}. \qquad (10)$$

The parameters which describe the GW source are:

$$\boldsymbol{\theta}_{\rm gw} = \{h_0, \iota, \psi, \delta, \alpha, , \Omega, \Phi_0\}, \qquad (11)$$

where h_0 is the characteristic wave strain, ι is the angle between the normal to the SMBHB orbital plane, $\boldsymbol{L}$, and the observer's line of sight, i.e. $\cos\iota = \boldsymbol{n}\cdot\boldsymbol{L}$, ψ the polarization angle of the GW and δ, α the declination and right ascension of the GW source respectively. The complete set of static parameters is denoted $\boldsymbol{\theta} = \boldsymbol{\theta}_{\rm psr} \cup \boldsymbol{\theta}_{\rm gw}$. There are $7+5N$ parameters to estimate, although the pulsar parameters are constrained better *a priori* by electromagnetic observations than the GW parameters. For example estimates of pulsar distances are accurate to $\sim 10\%$ (Cordes & Lazio 2002; Verbiest et al. 2012; Desvignes et al. 2016; Yao et al. 2017), but we have no prior information about δ and α.

3 INCLUSION OF THE PULSAR TERM

In this section we review the modification to Equation (8) used in K23, the issues that arise when using the full form of Equation (8) for likelihood-based inference, and a new parametrisation that alleviates these issues.

3.1 Earth term

Equation (8) is the sum of two equal amplitude, phase shifted waves. The first wave, $\cos(-\Omega t + \Phi_0)$, depends only on the GW source parameters and is shared across all pulsars. The argument of the cosine corresponds to the GW phase at the observer on Earth. Conversely the second wave, $\cos\left(-\Omega t + \Phi_0 + \Omega\left(1 + \boldsymbol{n}\cdot\boldsymbol{q}^{(n)}\right)d^{(n)}\right)$, also depends on $d^{(n)}$ and $\boldsymbol{q}^{(n)}$ and so varies between pulsars. The argument of the cosine corresponds to the GW phase at each the individual pulsar. The first and second terms are commonly referred to as the "Earth term" and "pulsar term" respectively. Whilst the Earth term is phase coherent between all pulsars and so can be summed across the array to increase the total signal-to-noise, the pulsar terms each have individual phases and in standard PTA analysis are typically considered as a source of self noise and dropped from the analysis (e.g. Sesana & Vecchio 2010; Babak & Sesana 2012a; Petiteau et al. 2013; Zhu et al. 2015b; Taylor et al. 2016; Goldstein et al. 2018; Charisi et al. 2023) at the expense of a modestly reduced detection probability ($\sim 5\%$) and the introduction of a bias in the sky localisation (Zhu et al. 2016; Chen & Wang 2022). K23 also followed this example and dropped the pulsar terms from the inference model. Explicitly the measurement equation used is

$$f_{\rm m}^{(n)}(t) = f_{\rm p}^{(n)}(t-d)g_{\rm Earth}^{(n)}(t), \qquad (12)$$

with

$$g_{\rm Earth}^{(n)}(t) = 1 - \frac{H_{ij}[q^{(n)}]^i[q^{(n)}]^j}{2[1 + \boldsymbol{n}\cdot\boldsymbol{q}^{(n)}]}\cos(-\Omega t + \Phi_0). \qquad (13)$$

3.2 Challenges of pulsar term

K23 uses a likelihood-based Bayesian framework for inference of the model parameters and model selection. That is, given a temporal sequence of noisy measurements $\boldsymbol{Y}$, the posterior distribution of $\boldsymbol{\theta}$ is calculated by Bayes' Rule,

$$p(\boldsymbol{\theta}|\boldsymbol{Y}) = \frac{\mathcal{L}(\boldsymbol{Y}|\boldsymbol{\theta})\cdot\pi(\boldsymbol{\theta})}{\mathcal{Z}}, \qquad (14)$$

where $\pi(\boldsymbol{\theta})$ is the prior distribution on $\boldsymbol{\theta}$ and $\mathcal{Z}$ is the marginalised likelihood, or evidence

$$\mathcal{Z} = \int d\boldsymbol{\theta} \mathcal{L}(\boldsymbol{Y}|\boldsymbol{\theta})\pi(\boldsymbol{\theta}). \qquad (15)$$

and $\mathcal{L}(\boldsymbol{Y}|\boldsymbol{\theta})$ is the likelihood calculated via a Kalman filter (Kalman 1960). Nested sampling (Skilling 2006) is used to estimate $p(\boldsymbol{\theta}|\boldsymbol{Y})$ and $\mathcal{Z}$. Given a specific realisation of $\boldsymbol{Y}$, $\mathcal{L}(\boldsymbol{Y}|\boldsymbol{\theta})$ is solely a function of $\boldsymbol{\theta}$, i.e. $\mathcal{L}(\boldsymbol{Y}|\boldsymbol{\theta}) = \mathcal{L}(\boldsymbol{\theta})$. We will use the notation $\mathcal{L}(\Theta)$ to refer to the likelihood returned by the Kalman filter for parameter Θ, where $\Theta \in \boldsymbol{\theta}$ and all other members of $\boldsymbol{\theta}$ are held constant at their true injected values.

To elucidate the complications introduced by including the pulsar term, we generate some noisy synthetic data $\boldsymbol{Y}$ using the methods outlined in K23. $\boldsymbol{\theta}_{\rm gw}$ are chosen arbitrarily, with $\alpha = 1.0$
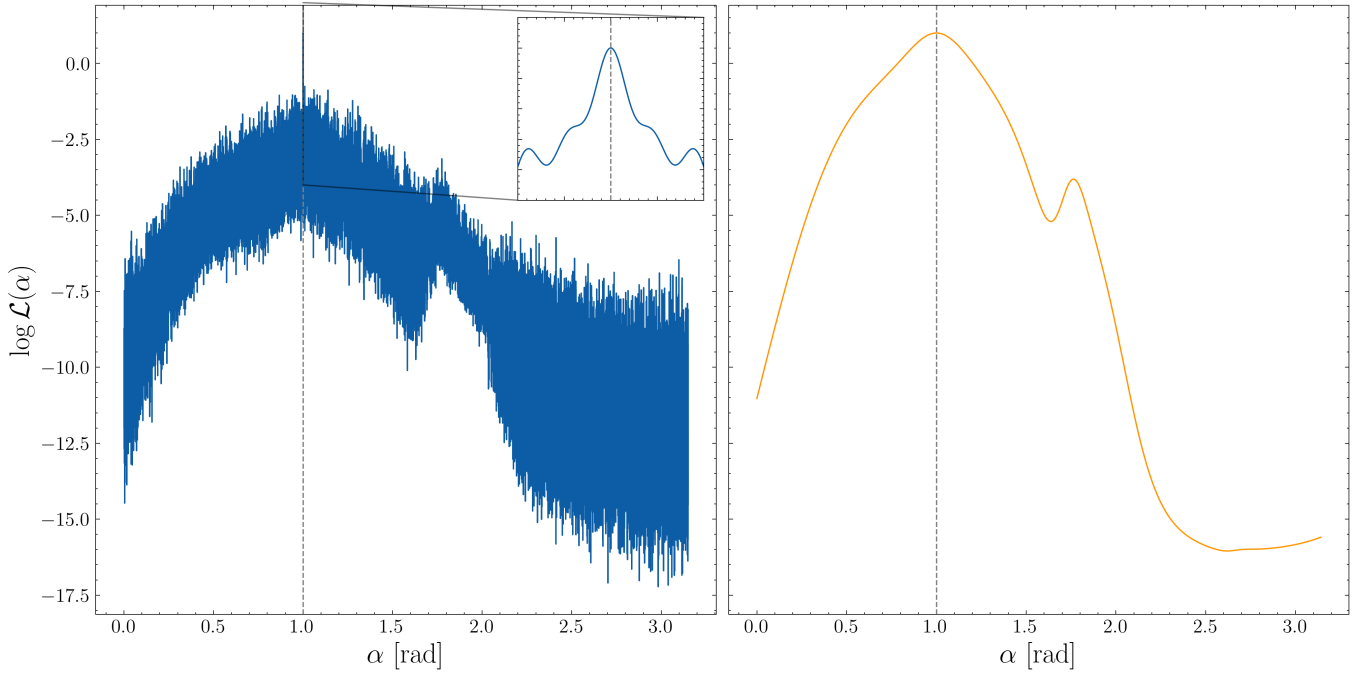
Figure 1. Logarithm of the one-dimensional likelihood $\mathcal{L}(\alpha)$ returned by the Kalman filter acting on synthetic data $\boldsymbol{Y}$. All other static parameters of $\boldsymbol{\theta}$ are held constant at their true injected values. In the left-hand panel the Kalman filter uses Equation (8) to calculate $\mathcal{L}(\alpha)$, i.e. inclusive of the pulsar terms. In the right-hand panel the Kalman filter uses Equation 13, i.e. just the Earth terms. The vertical dashed lines indicate the true injected value of α (= 1.0 rad) used to generate $\boldsymbol{Y}$. The inset plot covers the region $1.0 - 10^{-4} \leqslant \alpha \leqslant 1.0 + 10^{-4}$ rad. In the left hand panel $\mathcal{L}(\alpha)$ is very noisy, though a smooth concave optima exists on scales $O(10^{-4})$ rad. Conversely, in the right hand panel $\mathcal{L}(\alpha)$ is globally smooth.

rad. The choice of $\boldsymbol{\theta}_{\rm psr}$ corresponds to the 47 pulsars in the 12.5 year NANOGrav data set (Arzoumanian et al. 2020b). We run the Kalman filter using the measurement equation inclusive of the pulsar terms, Equation (8) on $\boldsymbol{Y}$ for different values of α, $0.0 \leqslant \alpha \leqslant \pi$ rad. We obtain a curve $\mathcal{L}(\alpha)$, which is plotted in the left hand panel of Figure 1 (blue curve). The dashed grey line indicates the injected value of α (= 1.0 rad). The inset plot shows a zoomed-in section of $\mathcal{L}(\alpha)$ within the region $1.0 - 10^{-4} \leqslant \alpha \leqslant 1.0 + 10^{-4}$ rad.

There are two important features to discuss in the left-hand panel of Figure 1. The first is that on scales of order the width of the prior $\pi(\alpha)$ (i.e radians), the curve of $\mathcal{L}(\alpha)$ is very noisy. Similar noisy curves are obtained for $\mathcal{L}(\Omega)$ and $\mathcal{L}(\delta)$. For all other static parameters, the $\mathcal{L}(\Theta)$ curves are smooth and globally concave. The second is that despite being noisy, a true likelihood maximum coincident with the injected value does exist and is locally concave on scales $O\left(10^{-4}\right)$ radians. This means that whilst it is theoretically possible to use likelihood-based methods for Bayesian estimation of α, in practice the computation is intractable since the noise in the likelihood curve inhibits sampling algorithms to reliably converge to a definitive posterior. Moreover, $\mathcal{L}(\alpha)$ is only a one-dimensional function. The challenge for sampling algorithms is further exacerbated when we consider the three-dimensional parameter space in $\alpha - \delta - \Omega$, or the full $7 + 5N$ dimensions of Section 2.3.

Why do α, δ and Ω exhibit noisy $\mathcal{L}(\Theta)$ curves whereas other static parameters do not? These parameters appear in the pulsar term as a product in the pulsar-dependent phase correction $\Omega\left(1 + \boldsymbol{n} \cdot \boldsymbol{q}^{(n)}\right) d^{(n)}$, where we remind the reader that $\boldsymbol{n} = \boldsymbol{n}(\delta, \alpha)$. Over the typical pulsar distances $d^{(n)} \sim 1$ kpc, a 10 nHz GW can ac-

cumulate 10^3 cycles. This creates a confusion problem when taking the cosine of $\Omega\left(1 + \boldsymbol{n} \cdot \boldsymbol{q}^{(n)}\right) d^{(n)}$ since we do not know how many cycles the wave has gone through, modulo 2π. TK: this explanation is rubbish! How can we say this better?. Conversely, if we drop the pulsar term, the $\mathcal{L}(\alpha)$ curve (as well as $\mathcal{L}(\Omega)$, $\mathcal{L}(\delta)$) This is shown by the orange curve in the right-hand panel of Figure 1 where we plot $\mathcal{L}(\alpha)$, analogous to the left-hand panel, but now use Equation 13 in our Kalman filter (i.e. just the Earth terms) rather than the full Equation 8. In this case there is no confusion regarding the number of cycles the wave has gone through over a distance $d^{(n)}$ and the curve is smooth.

3.3 New parametrisation

In order to include the pulsar terms in an inference model and apply the methods of K23 it is necessary to be able to handle the noisy likelihood curves presented in Section 3.2.

Whilst computational methods for approximate inference from noisy likelihoods do exists (e.g. Dunbar et al. 2022; Järvenpää & Corander 2021; Järvenpää et al. 2019)

Whilst noisy likelihood inference is possible...

In this section we introduce a new parametrisation of the model described in Section 2 in order to alleviate the problems outlined in Section 3.2.

We define a new parameter

$$\chi^{(n)} = \Omega\left(1 + \boldsymbol{n} \cdot \boldsymbol{q}^{(n)}\right) d^{(n)} \tag{16}$$

Such that Equation (8) becomes

$$g^{(n)}(t) = 1 - \frac{H_{ij}[q^{(n)}]^i[q^{(n)}]^j}{2[1 + \mathbf{n} \cdot \mathbf{q}^{(n)}]}$$
$$\times \left[\cos\left(-\Omega t + \Phi_0\right) \right.$$
$$\left. - \cos\left\{-\Omega t + \Phi_0 + \chi^{(n)}\right\} \right] . \tag{17}$$

and the static pulsar parameters to be inferred become

$$\boldsymbol{\theta}_{\text{psr}} = \left\{ \gamma^{(n)}, \sigma^{(n)}, f_{\text{em}}^{(n)}(t_1), \dot{f}_{\text{em}}^{(n)}(t_1), \chi^{(n)} \right\}_{1 \leqslant n \leqslant N} . \tag{18}$$

whilst $\boldsymbol{\theta}_{\text{gw}}$ remain unchanged.

In figure Xa we plot

Clearly there is a relation between abc. This will nbe becked and shown ti no be a problm in Section Y

4 REPRESENTATIVE EXAMPLE: SINGLE SMBHB SOURCE AND COMPARISON WITH EARTH TERMS

5 SIGNAL TRACKING, PARAMETER ESTIMATION AND MODEL SELECTION

In K1

The workflow presented in K1, hich we also follow here proceeds as follows

In this section we present a new method to infer $\boldsymbol{\theta}$ and calculate the marginal likelihood (i.e. the model evidence). In Section 5.1 we outline how noisy measurements of the pulsar frequency, $f_{\text{m}}^{(n)}(t)$, can be used to estimate the hidden state sequence, $f_{\text{p}}^{(n)}(t)$, using a Kalman filter. In Section 5.2 we demonstrate how to deploy the Kalman filter in conjunction with a nested sampling technique to perform Bayesian inference. Model selection and the specification of the null model are described in Section 5.3. A complete summary of the workflow is presented in Section 5.4. The method complements traditional PTA analyses because it does not assume a specific functional form (e.g. power law) for the power spectral density of the TOA fluctuations.

5.1 Kalman filter and likelihood

The Kalman filter (Kalman 1960) is

In this work we use the linear Kalman filter, which assumes a linear relation between $d\mathbf{X}/dt$ and $\mathbf{X}(t)$ (dynamics) and between $\mathbf{Y}(t)$ and $\mathbf{X}(t)$ (measurement), with $\mathbf{X}(t) = \{f_{\text{p}}^{(n)}(t)\}$ and $\mathbf{Y}(t) = \{f_{\text{m}}^{(n)}(t)\}$. Extension to non-linear problems is straightforward using either an extended Kalman filter (Zarchan & Musoff 2000), unscented Kalman filter (Wan & Van Der Merwe 2000) or particle filter (Simon 2006). Equations (5) and (??) are non-linear in the static parameters (e.g. $d^{(n)}$), even though they are linear in $\mathbf{X}(t)$ and $\mathbf{Y}(t)$. Hence inferring the static parameters is a non-linear exercise, to be tackled separately after the linear Kalman filter operates on the data for a fixed set of static parameters. Inference of the static parameters in Equations (5) and (??) by nested sampling is discussed in Section 5.2.

Implementation of the linear Kalman filter for the PTA state-space model in Section 3.2, including the full set of Kalman recursion relations is presented in Appendix A. At each discrete timestep indexed by $1 \leqslant i \leqslant M$, the Kalman filter returns an estimate of the state variables, $\hat{\mathbf{X}}_i = \hat{\mathbf{X}}(t_i)$, and the covariance of those estimates, $\mathbf{P}_i = \langle \hat{\mathbf{X}}_i \hat{\mathbf{X}}_i^{\text{T}} \rangle$, where the superscript T denotes the matrix transpose. The filter tracks the error in its predictions of $\mathbf{X}_i$ by converting $\hat{\mathbf{X}}_i$ into predicted measurements $\hat{\mathbf{Y}}_i$ via Equations (5) and (??) and comparing with the actual, noisy measurements $\hat{\mathbf{Y}}_i$. This defines a residual $\boldsymbol{\epsilon}_i = \mathbf{Y}_i - \hat{\mathbf{Y}}_i$, which is sometimes termed the innovation. The Kalman filter also calculates the uncertainty in $\boldsymbol{\epsilon}_i$ via the innovation covariance $\mathbf{S}_i = \langle \boldsymbol{\epsilon}_i \boldsymbol{\epsilon}_i^T \rangle$. The innovation and the innovation covariance are then used to correct the state estimate $\hat{\mathbf{X}}_i$ according to Equation (A8). For a fixed set of static parameters, the Kalman filter returns an estimate of the the state sequence $\hat{\mathbf{X}}_1, \ldots, \hat{\mathbf{X}}_M$ which minimizes the mean square error. We explain how to use this intermediate output to infer the optimal values of the static parameters $\boldsymbol{\theta}$ in Section 5.2

The Gaussian log-likelihood of obtaining $\mathbf{Y}_i$ given $\hat{\mathbf{X}}_i$ can then be calculated at each timestep from the Kalman filter output according to

$$\log \mathcal{L}_i = -\frac{1}{2} \left(N \log 2\pi + \log |\mathbf{S}_i| + \boldsymbol{\epsilon}_i^{\mathsf{T}} \mathbf{S}_i^{-1} \boldsymbol{\epsilon}_i \right) . \tag{19}$$

The total log-likelihood for the entire sequence is

$$\log \mathcal{L} = \sum_{i=1}^{M} \log \mathcal{L}_i . \tag{20}$$

Given $\mathbf{Y}_1, \ldots, \mathbf{Y}_M$, $\mathcal{L}$ is a function of the estimates $\hat{\boldsymbol{\theta}}$ of the static parameters passed to the Kalman filter, i.e. $\mathcal{L} = \mathcal{L}(\mathbf{Y}|\hat{\boldsymbol{\theta}})$. Similarly the estimates of the state and measurement variables, $\hat{\mathbf{X}}$ and $\hat{\mathbf{Y}}$, are functions of $\hat{\boldsymbol{\theta}}$. If $\hat{\boldsymbol{\theta}}$ is close to the true underlying parameters $\boldsymbol{\theta}$, then the errors in $\hat{\mathbf{X}}$ and $\hat{\mathbf{Y}}$ are minimized and $\mathcal{L}$ is maximised. This is illustrated with synthetic data in Figure ??. In the left column, a time series of $f_{\text{m}}^{(1)}(t)$ including Gaussian noise (middle panel, red curve) is generated from Equations (1)–(4), (16), and (17) for a single pulsar and fed into the Kalman filter along with the true static parameters $\hat{\boldsymbol{\theta}} = \boldsymbol{\theta}$. The Kalman filter recovers the evolution of $f_{\text{p}}^{(1)}(t)$ with high fidelity; the estimate of $\hat{f}_{\text{p}}^{(1)}(t)$ (left top panel, blue curve) overlaps almost perfectly with the true $f_{\text{p}}^{(1)}(t)$ (left top panel, green curve). The predicted state $\hat{f}_{\text{p}}^{(1)}(t)$ is converted into a predicted measurement $\hat{f}_{\text{m}}^{(1)}(t)$ (middle panel, magenta curve), which again overlaps almost perfectly with the true measurement. The residuals $\epsilon(t)$ between the true and predicted measurements are small ($\lesssim 0.1\%$) and normally distributed (left bottom panel). By contrast, in the right column, the exercise is repeated while passing slightly incorrect static parameters to the Kalman filter, where Ω has been perturbed from its true value by 20%. In this case the Kalman filter fails to track $f_{\text{p}}^{(1)}(t)$ accurately, as the discrepancy between the blue and green curves in the top panel of the right-hand column indicates. It similarly fails to predict $f_{\text{m}}^{(1)}(t)$ accurately, as shown by the discrepancy between the red and magenta curves in the middle panel, and the residuals are no longer distributed normally (right bottom panel).

5.2 Nested sampling

We can use the likelihood returned by the Kalman filter, Equation (20), in conjunction with likelihood-based inference methods to estimate the posterior distribution of

We estimate the posterior distribution and the model evidence through nested sampling (Skilling 2006) in this paper. Nested sampling evaluates marginalised likelihood integrals, of the form given by Equation (15), which also approximates the posterior by returning samples from $p(\boldsymbol{\theta}|\mathbf{Y})$. It does so by drawing a set of n_{live}

live points from $\pi(\boldsymbol{\theta})$ and iteratively replacing the live point with the lowest likelihood with a new live point drawn from $\pi(\boldsymbol{\theta})$, where the new live point is required to have a higher likelihood than the discarded point. The primary advantage of nested sampling is its ability to compute $\mathcal{Z}$, on which model selection relies. Nested sampling is also computationally efficient and can handle multi-modal problems (Ashton et al. 2022). For these reasons, it has enjoyed widespread adoption in the physical sciences, particularly within the cosmological community (Mukherjee et al. 2006; Feroz & Hobson 2008; Handley et al. 2015), neutron star astrophysics (Meyers et al. 2021a,b; Melatos et al. 2023), particle physics (Trassinelli 2019) and materials science (Pártay et al. 2009). For a review of nested sampling we refer the reader to Buchner (2021a) and Ashton et al. (2022). Multiple nested sampling algorithms and computational libraries exist. (e.g. Feroz & Hobson 2008; Feroz et al. 2009; Handley et al. 2015; Speagle 2020; Buchner 2021b). In gravitational wave research it is common to use the `dynesty` sampler (Speagle 2020) via the `Bilby` (Ashton & Talbot 2021) front-end library. We follow this precedent and use `Bilby` for all nested sampling Bayesian inference in this work.

The primary tunable parameter in nested sampling is n_{live}. A greater number of live points is advantageous for large parameter spaces and multi-modal problems, whilst the uncertainties in the evidence and the posterior scale as $O\left(n_{\text{live}}^{-1/2}\right)$. However the computational runtime scales as $O(n_{\text{live}})$. Ashton et al. (2022) offered a rule-of-thumb trade-off, where the minimum number of live points should be greater than the number of static parameters. Informal empirical tests conducted as part of this paper support the trade-off suggested by Ashton et al. (2022); we find typically that the true $\boldsymbol{\theta}$ is contained within the 90% credible interval of the derived 1D marginalised posteriors of $\hat{\boldsymbol{\theta}}$ for $n_{\text{live}} > 7 + 5N$ with $N \leqslant 50$. Unless stated otherwise we take $n_{\text{live}} = 1000$ for all results presented in this work.

5.3 Model selection

The evidence integral $\mathcal{Z}$ returned by nested sampling is the probability of the data $\boldsymbol{Y}$ given a model $\mathcal{M}_i$. We compare competing models via a Bayes factor,

$$\beta = \frac{\mathcal{Z}(\boldsymbol{Y}|\mathcal{M}_1)}{\mathcal{Z}(\boldsymbol{Y}|\mathcal{M}_0)} . \tag{21}$$

Throughout this work we take $\mathcal{M}_1$ to be the state-space model that includes the presence of a GW. $\mathcal{M}_0$ is the null model, which assumes no GW exists in the data. This is equivalent to setting $g^{(n)}(t) = 1$ in Equations (??) and (8). The Bayes factors we quote in this work therefore quantify whether the data supports evidence for a GW compared to there being no GW signal present.

5.4 Summary of workflow

For the reader's convenience we now summarise the workflow for a representative PTA analysis using the Kalman filter and nested sampler for parameter estimation and model selection:

(i) Specify a PTA composed of N pulsars
(ii) Obtain N data inputs $f_{\text{m}}^{(n)}(t)$, collectively labelled $\boldsymbol{Y}$
(iii) Specify a state-space model $\mathcal{M}$, with static parameters $\boldsymbol{\theta}$.
(iv) Specify prior distribution $\pi(\boldsymbol{\theta})$
(v) Sample n_{live} points from $\pi(\boldsymbol{\theta})$

(vi) For each live point:

   (a) Pass the sample $\boldsymbol{\theta}_{\text{sample}}$ to the Kalman filter.
   (b) Iterate over the input data using the Kalman filter and obtain a single log $\mathcal{L}$ value, Equation (20)

(vii) Remove the live point with the lowest likelihood value, log $\mathcal{L}_{\text{lowest}}$
(viii) Constrained sample a new live point from $\pi(\boldsymbol{\theta})$, subject to the requirement that the new likelihood log $\mathcal{L}_{\text{new}} > \log \mathcal{L}_{\text{lowest}}$, where log $\mathcal{L}_{\text{new}}$ is calculated via steps (a)–(b).
(ix) Nested sampler updates $p(\boldsymbol{\theta}|\boldsymbol{Y})$ and $\mathcal{Z}$
(x) Repeat steps (vii) - (ix) until convergence criteria are satisfied.

In order to compute β the above workflow is repeated for a different $\mathcal{M}$. The resulting $\mathcal{Z}$ values can then be compared. We remind the reader that the above workflow differs from a realistic PTA analysis in on important respect, namely that the data are input as frequency time series $f_{\text{m}}^{(n)}(t)$ instead of pulse TOAs. The generalization to TOAs is subtle and will be tackled in a forthcoming paper.

6 VALIDATION PROCEDURE WITH SYNTHETIC DATA

In this section we outline how synthetic data is generated in order to validate the analysis scheme in Section 5. In Section 6.1 we describe how to construct a representative synthetic PTA, and how to set astronomically reasonable values for the static pulsar parameters $\boldsymbol{\theta}_{\text{psr}}$. In Section 6.2 we demonstrate how to solve the equations of Section 2 for the synthetic PTA so as to generate noisy, frequency time series $f_{\text{m}}^{(n)}(t)$.

6.1 Constructing a synthetic PTA

We consider, by way of illustration, a synthetic PTA composed of the 47 pulsars in the 12.5 year NANOGrav dataset (Arzoumanian et al. 2020b). The NANOGrav pulsars are chosen arbitrarily as being representative of a typical PTA; the analysis below extends unchanged to any other PTA. For each pulsar we adopt the fiducial values for $q^{(n)}$, $d^{(n)}$, $f_{\text{em}}^{(n)}(t_1)$, and $\dot{f}_{\text{em}}(t_1)$, with the latter two quantities evaluated at the Solar System barycenter. A table of fiducial values is presented in Appendix B for the sake of reproducibility. The sky positions and colour-coded distances of the pulsars are displayed in Figure **??**. The pulsar parameters are acquired via the Australia Telescope National Facility (ATNF) pulsar catalogue (Manchester et al. 2005) using the `psrqpy` package (Pitkin 2018). The remaining static pulsar parameters are $\gamma^{(n)}$ and $\sigma^{(n)}$, for which no direct measurements exist. The ratio $\sigma^{(n)}/[\gamma^{(n)}]^{1/2}$ sets the typical root mean square fluctuations in $f_p^{(n)}(t)$, as discussed in Section 2.1 and the mean reversion timescale typically satisfies $[\gamma^{(n)}]^{-1} \gg T_{\text{obs}}$ (Price et al. 2012; Meyers et al. 2021a,b; Vargas & Melatos 2023). In this paper, for the sake of simplicity in the absence of independent measurements, we fix $\gamma^{(n)} = 10^{-13}$ s^{-1} for all n. We follow two complementary approaches in order to set physically reasonable values for $\sigma^{(n)}$. The first approach relies on the empirical timing noise model from Shannon & Cordes (2010b) which gives the standard deviation of the pulsar TOAs, $\sigma_{\text{TOA}}^{(n)}$, empirically as

$$\ln\left(\frac{\sigma_{\text{TOA}}^{(n)}}{\mu s}\right) = \ln \alpha_1 + \alpha_2 \ln f_p^{(n)} + \alpha_3 \ln\left(\frac{\dot{f}_p^{(n)}}{10^{-15}\text{s}^{-2}}\right)$$
$$+ \alpha_4 \ln\left(\frac{T_{\text{cad}}}{1 \text{ year}}\right) , \tag{22}$$

where T_{cad} is the cadence of the timing observations and for MSPs the best fit parameters are $\ln \alpha_1 = -20 \pm 20$, $\alpha_2 = 1 \pm 2$, $\alpha_3 = 2 \pm 1$, $\alpha_4 = 2.4 \pm 0.6$, for $\pm 2\sigma$ confidence limits. The uncertainties on these parameters are broad; for the purposes of generating astrophysically representative synthetic data we straightforwardly take the best fit parameter value. Throughout this work we assume that all pulsars are observed with a weekly cadence, $T_{cad} = 1$ week. In order to relate Equation (22), to $\sigma^{(n)}$ in Equation (4), we equate $\sigma^{(n)}$ to the root mean square TOA noise accumulated over one week, obtaining

$$\sigma^{(n)} \approx \sigma_{TOA}^{(n)} f_p^{(n)} T_{cad}^{-3/2} . \tag{23}$$

For the synthetic NANOGrav PTA depicted in Figure **??**, the median $\sigma^{(n)}$ calculated in this way is $\sigma^{(n)} = 5.51 \times 10^{-24}$ s$^{-3/2}$, $\min[\sigma^{(n)}] = 1.67 \times 10^{-26}$ s$^{-3/2}$ for PSR J0645+5158 and $\max[\sigma^{(n)}] = 2.56 \times 10^{-19}$ s$^{-3/2}$ for PSR J1939+2134

As a cross-check, we estimate $\sigma^{(n)}$ by solving Equation (4) numerically using the `baboo` package [1], generating a synthetic phase solution,

$$\varphi^{(n)}(t) = \int_0^t dt' f_p^{(n)}(t') , \tag{24}$$

and adjusting $\sigma^{(n)}$ iteratively to generate phase residuals which qualitatively (i.e. visually) resemble empirical phase residuals measured from real pulsars; see Section 2 in Vargas & Melatos (2023) for a successful example of this approach. We obtain empirical phase residuals from the NANOGrav 12.5 year wideband timing dataset (Pennucci & Collaboration 2020; Alam et al. 2021). A visual cross-check is sufficient for the purposes of this paper, where we seek broadly representative values for $\sigma^{(n)}$. In an analysis involving real PTA data, $\sigma^{(n)}$ would be estimated from the data jointly with the other static parameters in θ. In Figure **??** we compare the synthetic and empirical residuals for PSR J1939+2134, one of the 47 NANOGrav pulsars plotted in Figure **??**. We see that the synthetic and empirical residuals are qualitatively similar. For this pulsar the synthetic residuals were generated using $\sigma^{(n)} = 10^{-27}$ s$^{-3/2}$ which is $\ll$ than the value inferred from the noise model of Equations (22) and (23), using the best fit parameters, $\sigma^{(n)} = 2.56 \times 10^{-19}$ s$^{-3/2}$. This highlights how given the large uncertainties on the parameters of Equation (22) using the best fit values may be less appropriate for certain pulsars. If we set $\ln \alpha_1 = -38$ in Equation (22), close to its lower limit, then the estimated $\sigma^{(n)}$ for PSR J1939+2134 is $\sigma^{(n)} = 3.90 \times 10^{-27}$ which is in much better agreement with the value inferred from the residuals comparison method. This discrepancy between the two estimates of $\sigma^{(n)}$ is particular to PSR J1939+2134; for all other pulsars we find the two estimates of $\sigma^{(n)}$ are comparable to within a few orders of magnitude.

6.2 Generating a synthetic sequence of pulse frequencies

We generate N synthetic noisy time series of the measured pulse frequency $f_m^{(n)}(t)$, one for each pulsar $1 \leqslant n \leqslant N$, as follows:

(i) Integrate Equations (4)–(3) numerically for the synthetic PTA described in Section 6.1, to obtain random realizations of $f_p^{(n)}(t)$ for $1 \leqslant n \leqslant N$.

(ii) Map from $f_p^{(n)}(t)$ to $f_m^{(n)}(t)$ via Equations (5) and (**??**)

Equations (4)–(3) are solved by a Runge-Kutta Itô integrator implemented in the `sdeint` python package [2]. The static pulsar parameters θ_{psr} are completely specified for the synthetic PTA outlined in Section (6.1). For this work we consider all pulsars to be observed for $T_{obs} = 10$ years, uniformly sampled with a weekly cadence. The measurement noise covariance as defined in Equation (7) can be approximately related to the uncertainty in the pulse TOA, σ_{TOA}, as

$$\sigma_m \approx f_p^{(n)} \sigma_{TOA} T_{cad}^{-1} . \tag{25}$$

Although Equations (23) and (25) superficially resemble one another, they are distinct; Equation (23) deals with the timing noise intrinsic to the pulsar due to rotational irregularities, whereas Equation (25) handles the detector measurement noise. For a millisecond pulsar with $f_p^{(n)} \sim 100$ Hz observed with a weekly cadence and $\sigma_{TOA} \sim 1\mu$s Equation (25) implies $\sigma_m \sim 10^{-10}$ Hz. The most accurately timed pulsars might have $\sigma_{TOA} \sim 10$ ns or $\sigma_m \sim 10^{-12}$ Hz. Throughout this paper we fix $\sigma_m = 10^{-11}$ Hz and take it as known *a priori* rather than a parameter to be inferred. Note that whilst σ_m is the same for every pulsar, $f_m^{(n)}$ is modified by a different realisation of the measurement noise for each pulsar.

Finite precision arithmetic leads to numerical errors when solving Equations (4)–(3) in the regime $\sigma^{(n)} \Delta W_t \ll f_p^{(n)}$ relevant to PTAs, where ΔW_t labels an increment of Brownian motion (see Appendix A). To fix the problem, we subtract the deterministic frequency evolution and track the new variable, equivalent to a change of variables:

$$f_p^{*(n)} = f_p^{(n)} - f_{em}^{(n)} . \tag{26}$$

We similarly modify the measurement variable to be

$$f_m^{*(n)} = f_m^{(n)} - f_{em}^{\diamond(n)} , \tag{27}$$

where $f_{em}^{\diamond(n)}$ is a guess of the deterministic spin-down based on the pulsar ephemeris which is measured to high accuracy in practice by TEMPO2. For synthetic data we can set $f_{em}^{\diamond(n)} = f_{em}^{(n)}$ without loss of generality, but this is impossible generally for astronomical observations, because the spin-down ephemeris is only known approximately. Equation (5) is then updated to read

$$f_m^{*(n)}(t) = f_p^{*(n)}(t-d)g^{(n)}(t) - f_{em}^{(n)}(t-d)\left[1 - g^{(n)}(t)\right] . \tag{28}$$

We emphasise that this change of variables is a convenient device to bring the numerical values into a reasonable dynamic range without having to use excessively long floating point formats (e.g. long double, quadruple). It does not remove any degrees of freedom nor does it involve an approximation. In particular $f_{em}^{(n)}(t_1)$ and $\dot{f}_{em}^{(n)}(t_1)$ remain as static parameters but appear in the measurement equation (28) rather than the dynamical state equations, Equations 4–(3).

7 REPRESENTATIVE EXAMPLE: SINGLE SMBHB SOURCE

In this Section we apply the analysis scheme of Section 5 and the validation procedure of Section 6 to a PTA which is perturbed by a GW from an individual quasi-monochromatic SMBHB source. We remind the reader that the analysis in this paper targets a single SMBHB source. The analysis of a stochastic background composed

---

[1] https://github.com/meyers-academic/baboo

[2] https://github.com/mattja/sdeint

of the superposition of multiple sources is more challenging and is postponed to a forthcoming paper. In Section 7.1 we outline the priors chosen on θ. In Section 7.2 we apply the workflow of Section 5.4 to estimate θ, for a single realisation of the pulsar process noise and the measurement noise. We go on in Section ?? to extend this parameter estimation procedure to multiple realisations of the noise processes. In Section 7.3 we calculate the the detectability of the source as a function of h_0.

The static GW source parameters θ_{gw} used for this injection are selected to be astrophysically reasonable and representative. The injected θ_{gw} are summarised in the "Injected Values" column of Table 1. The static pulsar parameters θ_{psr} are as described in Section 6.1 and are also shown in Table 1.

7.1 Prior distributions

For the Bayesian methods used in this work, one must select reasonable priors, $\pi(\theta)$, for the complete set complete of static parameters. For $\pi(\theta_{\mathrm{gw}})$ we choose standard non-informative priors (e.g. Bhagwat et al. 2021) as summarised in Table 1. The choice of $\pi(\theta_{\mathrm{psr}})$ requires some additional discussion.

The parameters which govern the deterministic evolution of the pulsar spin frequency, $f_{\mathrm{em}}^{(n)}(t_1)$ and $\dot{f}_{\mathrm{em}}^{(n)}(t_1)$ are well-determined by existing radio timing observations. We can identify $f_{\mathrm{em}}^{(n)}(t_1)$ with the pulsar barycentric rotation frequency and $\dot{f}_{\mathrm{em}}^{(n)}(t_1)$ with the time derivative of barycentric rotation frequency quoted by pulsar observation catalogues. For the 12.5 year NANOGrav pulsars the median error in the barycentric rotation frequency is $\sim 7 \times 10^{-13}$ Hz, and in the time derivative of barycentric rotation frequency is $\sim 1.8 \times 10^{-20}$ s^{-2}. Whilst it is then clear that $f_{\mathrm{em}}^{(n)}(t_1)$, $\dot{f}_{\mathrm{em}}^{(n)}(t_1)$ are typically measured with very high precisions, for this work we adopt a broader uniform prior, $\pm 10^3 \epsilon_a^{(n)}$ either side of the true value, where $\epsilon_a^{(n)}$ is the error for that pulsar quoted in the ATNF catalogue and the subscript $a = \{f, \dot{f}\}$ identifies the error as being in $f_{\mathrm{em}}^{(n)}(t_1)$, or $\dot{f}_{\mathrm{em}}^{(n)}(t_1)$ respectively. In this way we can test how well our method performs without requiring exceptionally precise and accurate measurements of the pulsar parameters to be made *a priori*. Instead we consider the pulsar parameters similarly to the GW source parameters and estimate them optimally within a consistent framework. Adopting looser priors in this way allows us to subject our method to a more stringent test and confirm that we still accurately estimate GW parameters without highly accurate and precise initial estimates of $f_{\mathrm{em}}^{(n)}(t_1)$ and $\dot{f}_{\mathrm{em}}^{(n)}(t_1)$.

The pulsar distances $d^{(n)}$ are typically not as well constrained as $f_{\mathrm{em}}^{(n)}(t_1)$ and $\dot{f}_{\mathrm{em}}^{(n)}(t_1)$, with uncertainties typically on the order of $\sim 10\%$ (Arzoumanian et al. 2018; Yao et al. 2017). However for this work, whilst the pulsar distance is used when generating synthetic data, as is discussed in Section 7.2 the pulsar distance is not used for our inference model and so we do not need to set a prior on $d^{(n)}$. Similarly we do not set a prior on $\gamma^{(n)}$; since $[\gamma^{(n)}]^{-1} \gg T_{\mathrm{obs}}$ this means that $\gamma^{(n)}$ is effectively "unobservable" over the decadal timescales that we are interested in. That is, for T_{obs} =10 years the solution of Equation (4) is effectively independent of the choice of $\gamma^{(n)}$ as long as the condition $[\gamma^{(n)}]^{-1} \gg T_{\mathrm{obs}}$ is satisfied. It is therefore sufficient to consider $\gamma^{(n)}$ to be known *a priori* and set it at its true injected value. We briefly explored setting an uninformative prior on $\gamma^{(n)}$ over e.g. LogUniform($10^{-15}, 10^{-10}$)

s^{-1} as well as setting $\gamma^{(n)}$ at some fixed value away from the true injected value (e.g. set $\gamma^{(n)} = 10^{-14}$s^{-1} rather than 10^{-13}s^{-1}) but the results are unchanged. Regarding $\sigma^{(n)}$, the majority of pulsars in our synthetic PTA have $\sigma^{(n)} \sim 10^{-20} - 10^{-22}$ s$^{-3/2}$ as calculated from Equations (22) and (23). For these pulsars we set an uninformative broad prior of LogUniform($10^{-23}, 10^{-19}$ s$^{-3/2}$). The single exception is PSR J1939+2134 which has a particularly large $\dot{f}_{\mathrm{em}}^{(n)}(t_1)$ compared to the other pulsars in the array and so $\sigma \sim 10^{-16}$s$^{-3/2}$. For our artificial dataset we set $\sigma = 10^{-21}$s$^{-3/2}$ for this pulsar in order to bring the process noise for all pulsars into a consistent range that can be described by a single constrained prior.

Since we are not setting priors on $\gamma^{(n)}$ or $d^{(n)}$ this reduces the dimensionality of the parameter space to $7 + 3N$. We use the notation $\theta_{\mathrm{psr,reduced}}$ to refer to the reduced parameter space, c.f. Equation 18. Explicitly,

$$\theta_{\mathrm{psr,reduced}} = \left\{ f_{\mathrm{em}}^{(n)}(t_1), \dot{f}_{\mathrm{em}}^{(n)}(t_1), \sigma^{(n)} \right\}_{1 \leqslant n \leqslant N} . \quad (29)$$

All the injected static parameters and their corresponding priors for this representative example are summarised in Table 1.

7.2 Parameter estimation

Initially we consider a single noise realisation of the synthetic data for the representative example system described in Table 1. We apply the Kalman filter using Equation (12) in conjunction with nested sampling in order to infer the posterior distributions in each of the parameters. The results are shown in Figure 2 for the seven parameters of θ_{gw}. The histograms shown in the figure are the one-dimensional posteriors for each parameter, marginalized over the set of all other parameters, where the dashed vertical blue lines show the 0.16 and 0.84 quantiles and the solid orange line the true injection value. The two-dimensional contours denote the (0.5, 1, 1.5, 2)-sigma equivalent contours. It is evident that for this representative example with characteristic strain $h_0 = 5 \times 10^{-15}$ that we are able to estimate all the static parameters of the system using our method, with the injected value contained within the 90% credible interval for all of the parameters.

For some of the parameters the estimated posterior is approximately symmetric about the true injected value (e.g. Ω). In this case the posterior median and the injected value are approximately coincident. For other parameters (e.g. ι) the distribution is not symmetric about the injected value and the posterior median and the injected value are not coincident. The median value of the posterior for ι is shifted by ~ 0.35 rad relative to the injected value, although the injected value does still remain inside the 90% credible interval. Similar effects are seen, albeit with a smaller shift, in other parameters such as δ and α. For a single realisation of the noise it is not clear if this discrepancy is a systematic effect, i.e. a bias in the parameter estimate, or else just a random variation specific to this particular noise realisation. We explore this further in Section ?? and Section 9.1 and show that this is a bias that results from dropping the pulsar terms, similar to that reported in Zhu et al. (2016). Similar results are derived for the the $3N$ parameters of $\theta_{\mathrm{psr,reduced}}$ and the parameters are generally recovered unambiguously, but we do not display the resulting posterior distributions here since the inference of θ_{gw} is the main focus of this work. We are able to simultaneously estimate both θ_{gw} and $\theta_{\mathrm{psr,reduced}}$.

For each parameter in θ_{gw} we calculate W_1 between every pair of posteriors across our 10^3 noise realisations. The results are presented

	Parameter	Injected Values	Units	Prior
$\theta_{\rm gw}$	Ω	5×10^{-7}	Hz	LogUniform$(10^{-9}, 10^{-5})$
	α	1.0	radians	Uniform$(0, 2\pi)$
	δ	1.0	radians	Uniform$(-\pi/2, \pi/2)$
	ψ	2.50	radians	Uniform$(0, 2\pi)$
	Φ_0	0.20	radians	Uniform$(0, 2\pi)$
	h_0	5×10^{-15}	-	LogUniform$(10^{-15}, 10^{-9})$
	ι	1.0	radians	Uniform$(0, \pi)$
$\theta_{\rm psr}$	$f_{\rm em}^{(n)}(t_1)$	$f_{\rm ATNF}^{(n)}$	Hz	Uniform$\left(f_{\rm ATNF}^{(n)} - 10^3 \epsilon_f^{(n)}, f_{\rm ATNF}^{(n)} + 10^3 \epsilon_f^{(n)}\right)$
	$\dot{f}_{\rm em}^{(n)}(t_1)$	$\dot{f}_{\rm ATNF}^{(n)}$	s^{-2}	Uniform$\left(\dot{f}_{\rm ATNF}^{(n)} - 10^3 \epsilon_{\dot{f}}^{(n)}, \dot{f}_{\rm ATNF}^{(n)} + 10^3 \epsilon_{\dot{f}}^{(n)}\right)$
	$d^{(n)}$	$d_{\rm ATNF}^{(n)}$	m	-
	$\sigma^{(n)}$	$\sigma_{\rm sc}^{(n)}$	s$^{-3/2}$	LogUniform$(10^{-23}, 10^{-19})$
	$\gamma^{(n)}$	10^{-13}	s^{-1}	-

Table 1. Summary of injected static parameters used for generating synthetic data in the representative example of Section 7, along with the choice of prior used for Bayesian inference on each parameter. The subscript "ATNF" denotes values which have been obtained from the ATNF pulsar catalogue as described in Section 6.1. The subscript "sc" indicates that the injected value has been calculated using the empirical timing model, Equations (22) and (23) from Shannon & Cordes (2010a). The quantities $\epsilon_f^{(n)}$ and $\epsilon_{\dot{f}}^{(n)}$ are the errors in $f_{\rm em}^{(n)}(t_1)$ and $\dot{f}_{\rm em}^{(n)}(t_1)$ respectively, as quoted in the ATNF catalogue.

in Figure **??**. The figure shows a lower triangular heat-map where each point denotes the W_1 value between a pair of posteriors. Small values of W_1 are magenta moving to red for large values of W_1. Note that the heat-map colour scaling is not the same for all subplots of the figure. It is evident that W_1 is generally small across all pairs of posteriors. We define $W_{1,\rm median}$ as the median value of W_1 across all $\binom{10^3}{2}$ pairs of noise realisations. The values of $W_{1,\rm median}$ for each parameter are quoted in Table **??**. As a percentage of the width of the prior space (e.g. for α the width of the prior is 2π), the median W_1 for each parameter is $\lesssim 3\%$. Generally speaking, the method converges to consistent one-dimensional posteriors for each parameter across different noise realisations.

There are a small fraction of the total number of noise realisations which have a large Wasserstein distance from all the other posteriors of all the other noise realisations. These are the strong yellow lines in Figure **??**. These correspond exclusively to posteriors which have converged poorly and not found the likelihood global maximum. For instance, the top strong horizontal yellow line in Figure **??**, which is identified by an asterisk in the figure, corresponds to a posterior for ψ which has converged sub-optimally, with an estimated value of $\psi = 1.01 \pm 0.06$ rad, highly diverged from the true injected value of 2.50 rad. The W_1 value between this posterior and all the posteriors inferred for all other noise realisations is ~ 1.7 radians. We also observe a strong correlation across all noise pairs (Pearson correlation coefficient = 0.96) between the W_1 inferred for α and ψ, indicating that noise realisations which corrupt the inference of ψ similarly affect α. This is due to multimodal likelihood surface for $\psi - \alpha$, shown in Figure **??**. We can see that the likelihood surface has a global optima at the approximate location of the injected values ($\alpha \sim 1.0$, $\psi \sim 2.5$) and local optima that corresponds to the location of the example poorly converged posterior discussed previously, with $\psi = 1.01$ rad. This problem of poor global convergence can be solved in principle by increasing the number of live points $n_{\rm live}$ in the nested sampler so as to better cover the likelihood surface and prevent falling into local minima.

7.3 Detection

We frame the problem of claiming a detection of a GW in the noisy data in terms of a Bayesian model selection procedure as described in Section 5.3. $\mathcal{M}_1$ is the Earth-terms only model, i.e. the state-space model with a Kalman filter using Equation (12). The Bayes factor, β, as defined in Equation (21) is presented in Figure 3 for our representative system, where we now vary the magnitude of the GW strain, h_0. The noise processes in the synthetic data are identical realisations for each value of h_0; the only change in the data is the change in h_0. We can see that for $\beta > 10$ there is an approximate log-linear relationship between β and h_0 where the GW source is easily detectable with decisive evidence ($\beta \sim 100$) for $h_0 \gtrsim 10^{-14}$. We take $\beta = 10$ as a tolerance cut-off above which we can accept $\mathcal{M}_1$ and claim a detection of the GW. For this system, given this realisation of the noise, the minimal detectable strain is $\sim 3.9 \times 10^{-15}$. This minimal detectable strain is of course particular to this system and will be influenced in general by e.g. $T_{\rm obs}$, $\sigma_{\rm m}$ as well as the parameters of the GW source such as its location on the sky.

There is an evident sparsity and steep drop-off of β for values of $h_0 \lesssim 3.9 \times 10^{-15}$. The steep drop off is due to the two competing models becoming increasingly indistinguishable as the strain signal decreases and the measurement noise starts to dominate. The sparsity is due some of the β value becoming negative at these points. This is a noise artefact of the nested sampling method. For these points the noise in the sampler starts to dominate, the sampler converges sub-optimally, and the hierarchical relationship between $\mathcal{M}_0$ and $\mathcal{M}_1$ fails. That is, the requirement that $\mathcal{Z}(Y|\mathcal{M}_1) > \mathcal{Z}(Y|\mathcal{M}_0)$ no longer holds. There is nothing special about these particular points; if one recreates the $\beta - h_0$ curve by rerunning the nested sampler these sparse locations appear at different values of h_0, for $\beta < 10$. For $\beta > 10$ the sampling noise is sufficiently small with respect to the signal and the model hierarchy holds. Increasing the number of live points $n_{\rm live}$ used by the nested sampler improves the performance at small values of h_0 since as discussed in Section 5.2 the uncertainties in $\mathcal{Z}$ scale as $\mathcal{O}(1/\sqrt{n_{\rm live}})$. For the results presented in this subsection we set $n_{\rm live} = 2000$.
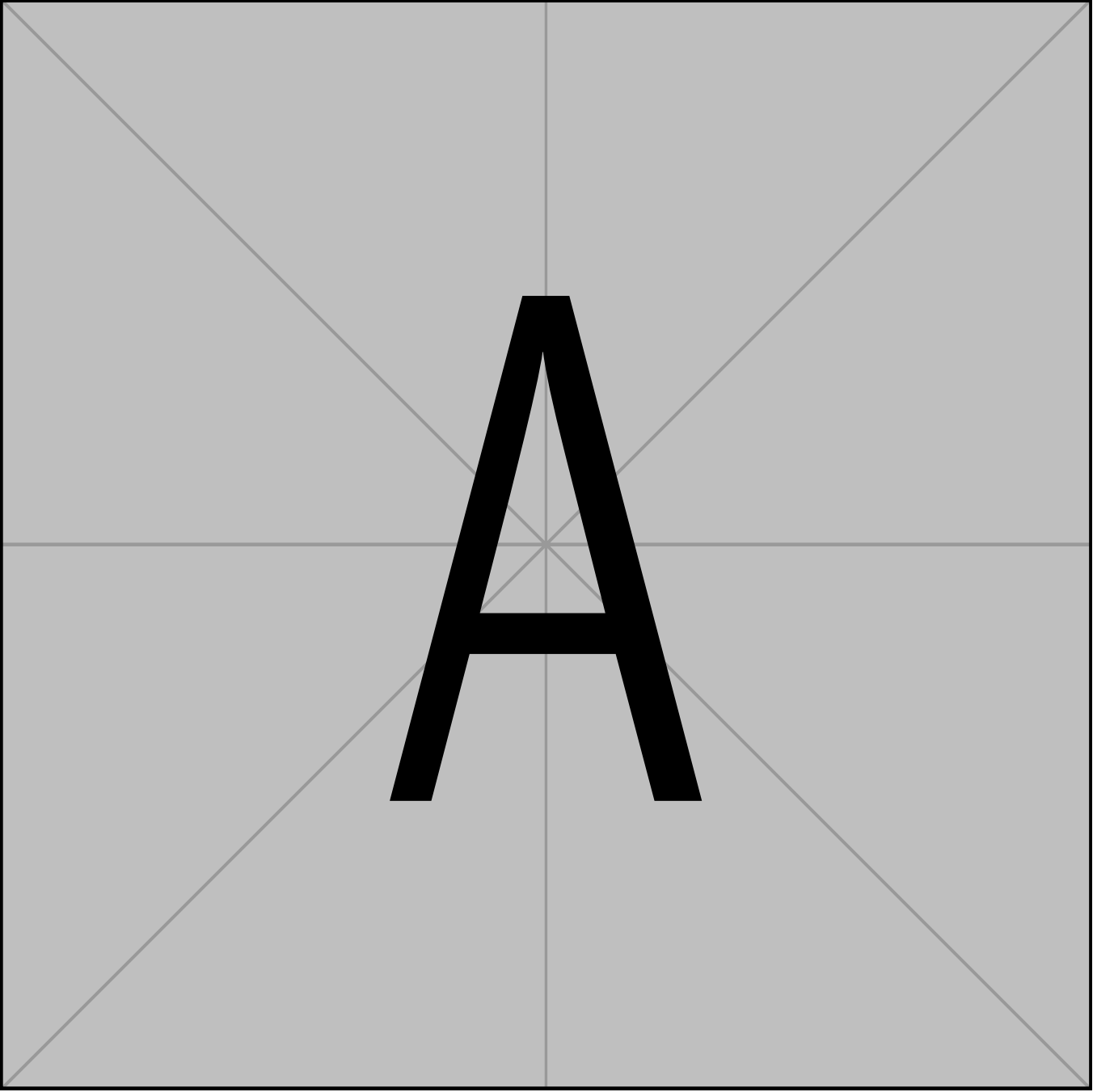
Figure 2. Posterior distribution for the GW source parameters $\theta_{\rm gw}$ for the representative system described in Table 1, for a single realisation of the system noise. The vertical orange lines indicate the true injected values. The contours in the 2D histograms denote the (0.5, 1, 1.5, 2)-σ levels. The subtitles of the marginalized 1D posteriors denote the posterior median and the 0.16,0.84 quantiles. We are able to accurately estimate each parameter of interest. We plot the scaled variables $\Omega_{\rm nHz} = \Omega \times 10^9$ Hz and $h_{0, \times 10^{15}} = h_0 \times 10^{15}$. Note that the x-axis scaling does not span the total prior space.
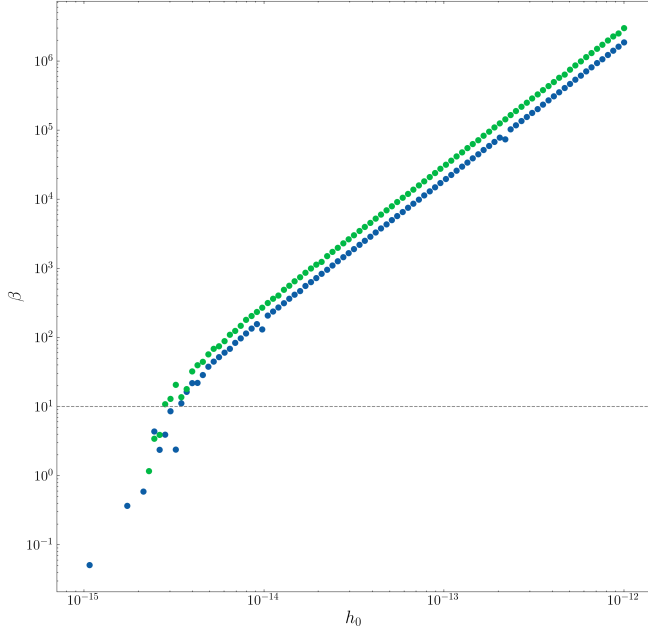
Figure 3. Bayes ratio β between the competing models $\mathcal{M}_1$ (GW present in data) and $\mathcal{M}_0$ (GW not present in data) at different GW strain magnitudes , h_0, for the representative example summarised in Table 1. The horizontal grey dashed line labels the detection threshold of $\beta = 10$. The minimal detectable strain, below which $\beta < 10$, is $\sim 3.9 \times 10^{-15}$. Gaps in the data below $\beta = 10$ occur due to noise in the sampler breaking the hierarchical relationship between $\mathcal{M}_0$ and $\mathcal{M}_1$.

8 EXPLORING A BROADER PARAMETER SPACE

We have so far focussed on a single representative system, summarised in Table 1. In this section we test the method in different regions of the parameter space, varying the source parameters through astrophysically relevant ranges.

We consider 200 injections for different sets of parameter values where we fix $h_0 = 5 \times 10^{-15}$, $\iota = 1.0$ and draw the remaining five parameters of $\boldsymbol{\theta}_{\mathrm{gw}}$ from the prior distributions described in Table 1. We fix h_0 and ι in order to maintain an approximately constant SNR across the parameter space. For each simulated injection we can then attempt to recover the posterior distributions for each parameter. To summarise the results across the parameter space we use a parameter-parameter (PP) plot (Cook et al. 2006). A PP plot describes the fraction of the total number of injected parameters which are included within a given credible interval of the estimated posterior with respect to the credible interval itself. In the ideal case the PP plot should be a diagonal line, indicating that x-percentage of the simulated injections fall within the x-percentage credible interval. The results are shown in Figure 4. The shaded grey contours enclose the 1σ, 2σ, and 3σ significance levels, given 200 injections. We can see that only Ω falls within the 3σ shaded region. The other parameters deviate from the $y = x$ diagonal. The effect is most pronounced for α and δ with more modest deviations for ψ and Φ_0. The shape of the graph indicates that the posteriors for these parameters are overconstrained; there are fewer injections contained within high value credible intervals than would be expected statistically, and there are more injections contained within the low value credible intervals. This is an result of the bias that we observed in Section **??**; the posteriors inferred for these parameters are generally confident, but are systematically biased away from the true injection values. This manifests in the PP plot as posteriors which are overly precise (narrow) to contain the injected value within the appropriate credible interval. An in-depth discussion on the origin of this bias is given in Section 9.1.
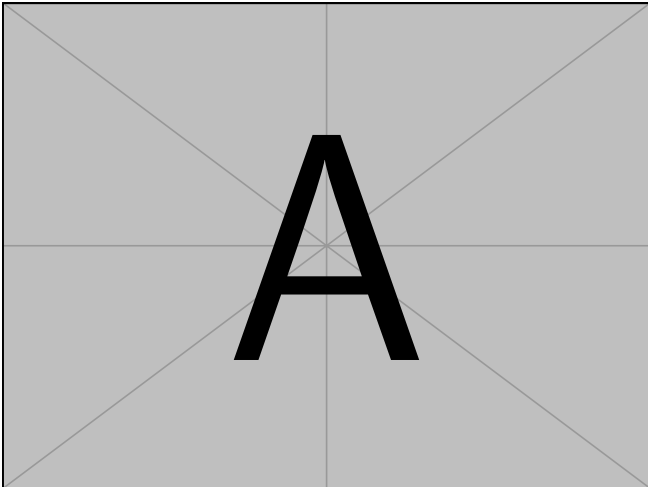
Figure 4. PP plot for 200 simulated GW sources for a subset of parameters of $\boldsymbol{\theta}_{\mathrm{gw}}$, randomly drawn from the prior distributions of Table 1. Each coloured line corresponds to a different parameter of $\boldsymbol{\theta}_{\mathrm{gw}}$. The parameters h_0 and ι are fixed at 5×10^{-15} and 1.0 rad respectively in order to maintain an approximately constant SNR. The grey shaded contours labels the 1, 2, 3-σ confidence intervals. Well estimated posteriors should fall along the diagonal $y = x$. Ω is generally well-estimated but many other parameters show evidence of being over-constrained due to a modelling bias.

9 IDENTIFIABILITY AND BIAS

There are two underlying issues in the preceding tests that we now explore in more detail. The first relates to parameter identifiability, i.e. can we uniquely identify the parameters of the model given the data and the model structure? This question is explored in Section **??**. The second relates to a bias in the parameter estimates that results from dropping the pulsar terms from the Kalman filter measurement equation as described in Section 7.2. This is the focus of Section 9.1. In order to elucidate these questions without confusion from the measurement noise, we now work in the high SNR regime and set $h_0 = 10^{-12}$ (c.f. Figure 3) for our representative example system (Table 1). [3]

9.1 Bias by dropping pulsar terms

Evident in the preceding discussion is the fact that for some of the $\boldsymbol{\theta}_{\mathrm{gw}}$ parameters the inferred value (e.g. the median of the one-dimensional marginalised posterior) is biased away from the true injection value. In Figure **??** we show the resulting posteriors for $\boldsymbol{\theta}_{\mathrm{gw}}$, analogous to Figure 2, but now for the high-SNR system with $h_0 = 10^{-12}$. We can see that for all parameters, with the exception of Ω and h_0, the injected value lies outside the 90% credible interval, to the extent that it is not visible on the scales over which we have plotted the posteriors. This effect is most severe for ι with a bias of ~ 0.3 rad but is also present to a lesser extent in other static parameters such as δ, α and ψ, and additionally to an even smaller extent in Φ_0. Similar results are obtained for other noise realisations. Whilst h_0 does not exhibit any noticeable bias for this particular noise realisation, in general across multiple noise realisations it does exhibit a correlated bias with ι. In this Section we demonstrate how this bias results from the dropping of the pulsar terms described in Section 7.2.

In Figure **??** we plot the variation in the log-likelihood returned by the Kalman filter, Equation (20), as we vary ι across the prior space, holding all other parameters constant at the true injected value of the representative example system, Table 1. We do this for 10 separate realisations of the system noise. We consider three separate situations: *(i)* The solid blue line is the likelihood curve with just the Earth-terms included (i.e. using Equation 12 in the Kalman filter), *(ii)* the solid orange line is the likelihood curve with the additional pulsar terms included (i.e. using Equation 5), *(iii)* the solid green line is the solution where we drop the pulsar terms from both the synthetic data and the measurement equation. We have not used nested sampling for situations *(ii)* or *(iii)* in this work. However, we are able to run the Kalman filter either using the pulsar terms in the model or else dropping them from the synthetic data consider how the resulting likelihood varies for different parameter values. The dashed lines show the location of the likelihood maxima for each of the likelihood solutions; finding the location of the maxima across all static parameters is effectively the goal of any likelihood based inference method, such as nested sampling.

The key observation from Figure **??** is that for the Earth-terms only solution the location of the likelihood optima and the location

---

of the injected value are not the same. Consequently Bayesian likelihood inference techniques settle in optima that do not necessarily align with the true injection value. This is the origin of the bias in the one-dimensional marginalised posteriors that we observe. For the Earth-terms solution the optima of the likelihood curve lies around $\iota \sim 0.7$ radians, whereas the injected value was $\iota = 1.0$ radians. This optima is comparable to the median of the posterior inferred for ι in Figure **??**.

In contrast to the Earth-terms solution, for the pulsar-terms solution the optima of the likelihood curve now aligns with the true injected value. The corollary is also true; if we drop the pulsar terms from the synthetic data and use the Earth terms equation for inference then the optima is also correctly located. This evidences that it is the effect of dropping the pulsar terms from the measurement equation which causes this bias in the inferred posteriors. Similar results are observed for the other parameters which exhibit a bias in the nested sampling inference.

Why does dropping the pulsar terms bias these parameters in particular, whilst leaving others unaffected? For instance, why is the bias induced in ι so strong, whereas ψ shows only a weak bias and Ω shows no bias at all? When we generate synthetic data including the pulsar term, the state frequency of an individual pulsar f_p is effective modulated by the interference of two equal-amplitude, phase shifted waves (c.f. Equation 5). Explicitly, we have the "Earth-terms wave" with a general form $y_{Earth} = A \cos \xi$ for amplitude A and phase ξ and the "pulsar-terms wave" with a general form $y_{pulsar} = A \cos(\xi + \kappa)$ for phase offset κ. The net interference wave that modulates f_p is

$$y_{Earth} - y_{pulsar} = 2A \sin\left(\frac{\kappa}{2}\right) \sin\left(\xi + \frac{\kappa}{2}\right) . \qquad (30)$$

The additional modulations from y_{pulsar} influence the amplitude of the resulting interference wave, but do not affect its frequency. When we model this data using the Kalman filter without the pulsar terms, the additional amplitude modulations from y_{pulsar} must be described by the single wave model, y_{Earth}. As a result the y_{Earth} model must try to compensate for these amplitude modulations by adjusting the parameters which govern the amplitude of the single wave. Consequently the parameters which are most affected are those which determine the amplitude of the GW. Terms which influence the amplitude strongly, such as h_0 and ι, are strongly affected and exhibit a strong bias. Terms which influence the amplitude weakly such as ψ exhibit a weaker bias. The wave amplitude is independent of the frequency and so Ω exhibits no bias. Since a shift in phase affects the instantaneous amplitude of the wave, Φ_0 also exhibits a small bias, despite A not being a function of Φ_0. This hierarchy of biases for each parameter is also what we observe in Figure 4, where α and δ are strongly over-constrained whilst Ω is well-estimated.

In order to ascertain how important the bias is for PTA continuous wave searches requires a thorough exploration of the astrophysical parameter space which we do not carry out in this work. The magnitude of the bias will vary for different points in the parameter space, as well as for different PTA configurations. If the bias is sufficiently modest then for quiet continuous wave sources with low SNR the uncertainty in the one-dimensional marginalised posterior may dominate and the bias may not be important for searches. This is what we observe for our synthetic data (e.g. Figure **??**); the decreased SNR manifests as a broader marginalised posterior which generally overwhelms the shift due to the bias. Conversely if the bias is sufficiently strong, or the source sufficiently loud with low

uncertainties, then the bias may come to systematically affect the inferred parameters.

We have shown in this section how the dropping of the pulsar terms results in a bias in the inferred parameters, not just in the sky localisation parameters (e.g. Zhu et al. 2016; Chen & Wang 2022) but additionally all parameters which influence the wave amplitude. Whilst the bias is generally small and does not prevent the recovery of accurate posteriors for our example system, it is present and may need to be accounted for for analysis in other parts of the parameter space. This bias is not particular to our method but a shared feature across likelihood based methods that do not include the pulsar terms in the inference model. The inclusion of the pulsar terms in the methods presented in this work in order to alleviate the bias will be a key goal of a future work.

10 DISCUSSION

We have shown how our complementary approach to PTA data analysis using a Kalman filter can successfully recover the underlying parameters of the model and calculate Bayes factors in order to perform Bayesian model selection. There are a number of potential extensions of this work which we now discuss.

The natural first extension is to implement the method whilst retaining the pulsar terms of Equation 5. Whilst PTA searches commonly drop the pulsar terms as standard practice, we have shown that this leads to biases in the inferred one-dimensional marginalized posteriors for the model parameters. Biases in sky localisation for synthetic datasets as a result of dropping the pulsar terms are also observed by Zhu et al. (2016) and Chen & Wang (2022). Alternatively, if the method continues to be used with solely the Earth terms then it would be highly desirable to make systematic, quantitative estimates of the incurred biases in the model parameters across an astrophysically representative parameter space.

We have considered only a specific configuration of pulsars composing our synthetic PTA - the same pulsars that make up the 12.5-year NANOGrav (Section 6.1). Whilst our method is generally independent of the specific choice of pulsars, it would be of interest to compare the performance of the method using different pulsars configurations and different PTAs such as PPTA and the EPTA. Indeed, since adding pulsars to PTAs increases the computational demands of the data analysis it may be advantageous to optimally select a subset of the total available pulsars which may be able to provide comparable performance to a larger PTA (Speri et al. 2023).

Throughout this work we have assumed that all pulsars are observed at the same time, with a constant time sampling. In practice this assumption does not hold and different pulsars will be observed with different cadences at different times. Extending this method to non-constant time sampling is straightforward and the performance of the method should be evaluated in this regime.

We have taken our GW source to be monochromatic, i.e. Ω is a fixed parameter with no time dependence. Whilst this is an astronomically well-justified assumption (see discussion in Section **??**), and appropriate for this initial methods work, it would also be of interest to extend the state-space construction to enable the GW frequency to evolve in time. The GW source is monochromatic over the decadal PTA observation period, but the timescale set

by the Earth-pulsar distance is comparable to the SMBHB evolution timescale (Sesana & Vecchio 2010). For $\Delta f_{\mathrm{gw}} < 1/T_{\mathrm{obs}}$ (see Equation (9)) the GW source frequency evolution manifests as an incoherent source of noise in the pulsar terms, whilst for $\Delta f_{\mathrm{gw}} > 1/T_{\mathrm{obs}}$ the pulsar terms can affect the phase coherency of the Earth terms (Perrodin & Sesana 2018). Careful consideration of the evolution of the GW frequency will be important as we look to extend our method to include the pulsar terms in the inference model.

We have also assumed that there is only a single GW source that influences the received pulsar frequencies. However, it may be possible to resolve multiple continuous GW sources concurrently (Babak & Sesana 2012b). Our method naturally extends to detecting multiple GW sources simultaneously; Equation (5) is straightforwardly modified to become a linear superposition of multiple GWs. The stochastic background itself is the incoherent summation of many individual GW sources. It therefore stands to reason that it may be possible to extend this method to also search for a stochastic GW background, providing a complementary approach to detect the stochastic background without requiring a cross-correlation of the pulsar residuals to uncover the Hellings-Downs curve.

TK: Lets also pre-empt reviewer and make it explicit why we are using frequencies rather than TOAs. Need to chat with group to get this clear in my head.

11 CONCLUSION

In this paper we demonstrate a new method for the detection and parameter estimation of GWs from individual, monochromatic SMBHBs. We track the evolution of the intrinsic pulsar timing noise explicitly via a state-space method, rather than subtracting the ensemble-averaged statistics. That is, we disentangle statistically the specific time-ordered realisation of the timing noise from the GW induced modulations. This enables the inference of GW parameters conditioned on the specific observed realisation of the noisy data. We introduce the Kalman filter in order to track the intrinsic state evolution of the pulsar and combine this with a Bayesian sampling framework to estimate the posterior distributions of each parameter of the system, as well as the associated evidence (marginalised likelihood) of the model. We test our method on synthetic data. We initially focus on a single, astrophysically representative, SMBHB GW source detected with the 12.5-year NANOGrav pulsars observed over a 10 year timespan. The parameters of the model are accurately recovered and the minimal detectable strain is estimated to be $h_0 \sim 4 \times 10^{-15}$ for $\iota = 1.0$ rad. The method is then further tested over 1000 noise realisations. Consistent posterior estimates of the parameters are obtained for the majority of noise realisations, with the median Wasserstein distance across all noise realisations $W_{1,\mathrm{median}}$ generally small compared to the prior space ($\lesssim 3\%$). For a minority of noise realisations the nested sampler converges poorly and settles into a local likelihood optima for the posteriors estimates of ψ and α. This problem can be solved in general by increasing the number of live points n_{live} used by the sampler. Exploration of a broader parameter space via 200 randomly sampled parameter vectors highlights biases in some parameters as a result of dropping the pulsar terms from the inference model. The cause of these biases is examined for the case of high SNR, along with the structural weak-identifiability between ι and h_0. The extension of this method to include the pulsar term is a key challenge for a future work.

APPENDIX A: KALMAN RECURSION EQUATIONS

The linear Kalman filter operates on temporally discrete, noisy measurements Y_k, which are related to a set of unobservable discrete system states X_k, via a linear transformation:

$$Y_k = H_k X_k + v_k , \tag{A1}$$

where H_k is the measurement matrix or observation model, v_k is a zero-mean Gaussian measurement noise, $\mathcal{N} \sim (0, R_k)$ with covariance, and the subscript k labels the time-step. The Kalman filter takes the underlying states to evolve according to

$$X_k = F_k X_{k-1} + G_k u_k + w_k , \tag{A2}$$

where F is the system dynamics matrix, G the control matrix. u the control vector, and w_k is a zero-mean Gaussian process noise, $\mathcal{N} \sim (0, Q_k)$.

The Kalman filter is a recursive estimator with two distinct stages; a "predict" stage and an "update" stage. The predict stage predicts the estimate of the state at discrete step k, given the state estimates from step $k - 1$. Specifically, the predict step proceeds as,

$$\hat{X}_{k|k-1} = F_k \hat{X}_{k-1|k-1} + G_k u_k \tag{A3}$$

$$\hat{P}_{k|k-1} = F_k \hat{P}_{k-1|k-1} F_k^{\mathsf{T}} + Q_k \tag{A4}$$

Note that the predict stage is independent of the measurements. The measurement Y_k is included to update the prediction during the update stage as follows:

$$\epsilon_k = Y_k - H_k \hat{X}_{k|k-1} \tag{A5}$$

$$S_k = H_k \hat{P}_{k|k-1} H_k^{\mathsf{T}} + R_k \tag{A6}$$

$$K_k = \hat{P}_{k|k-1} H_k^{\mathsf{T}} S_k^{-1} \tag{A7}$$

$$\hat{X}_{k|k} = \hat{X}_{k|k-1} + K_k \epsilon_k \tag{A8}$$

$$\hat{P}_{k|k} = (I - K_k H_k) \hat{P}_{k|k-1} \tag{A9}$$

Equation (A7) defines the "Kalman gain" K_k which is defined so as to minimise the mean squared error in the state estimate, i.e. $K_k = \mathrm{argmin}\left[E(X_k - \hat{X}_k) \right]$. For a full review of the Kalman filter, including its derivation, we refer the reader to Gelb et al. (1974) and Zarchan & Musoff (2000).

We map our continuous-time state-space model described in Section 2 onto the discrete-time Kalman filter structure of Equations (A1), (A2) as follows. We identify X with a vector of length N composed of the intrinsic pulsar frequency states, i.e

$$X = \left(f_{\mathrm{p}}^{(1)}, f_{\mathrm{p}}^{(2)}, ..., f_{\mathrm{p}}^{(N)} \right) . \tag{A10}$$

Similarly,

$$Y = \left(f_{\mathrm{m}}^{(1)}, f_{\mathrm{m}}^{(2)}, ..., f_{\mathrm{m}}^{(N)} \right) \tag{A11}$$

The states evolve according the continuous dynamical equation (c.f. Equation (1))

$$dX = AX dt + C(t)dt + \Sigma dB(t) \tag{A12}$$

where A is a diagonal $N \times N$ square matrix

$$A = \text{diag}\left(\gamma^{(1)}, \gamma^{(2)}, ..., \gamma^{(N)}\right) , \tag{A13}$$

and $C(t)$ a time dependent vector with n-th component

$$C^{(n)} = \gamma^{(n)}\left(f_{\text{em}}^{(n)}(t_1) + \dot{f}_{\text{em}}(t_1)^{(n)}t\right) + \dot{f}_{\text{em}}(t_1)^{(n)} . \tag{A14}$$

The $N \times N$ square matrix $\boldsymbol{\Sigma}$ governs the magnitude of the increments of Brownian motion (Wiener process) $dB(t)$, where

$$\boldsymbol{\Sigma} = \text{diag}\left(\sigma^{(1)}, \sigma^{(2)}, ..., \sigma^{(N)}\right) \tag{A15}$$

The evolution of the state is an Ornstein-Uhlenbeck process, described by a Langevin equation, Equation (A12), which has a general solution given by (Gardiner 2009),

$$X(t) = e^{At}X(0) + \int_0^t e^{A(t-t')}C(t')dt' + \int_0^t e^{A(t-t')}\boldsymbol{\Sigma}dB(t') \tag{A16}$$

From Equation (A16) we can construct the discrete, recursive solution for $X(t_k) = X_k$ in the form of Equation (A2) where

$$F_k = e^{A(t_{k+1}-t_k)} \tag{A17}$$

$$G_k = \int_{t_i}^{t_{i+1}} e^{A(t_{k+1}-t')}C(t')dt' \tag{A18}$$

$$w_k = \int_{t_k}^{t_{k+1}} e^{A(t_{k+1}-t')}\boldsymbol{\Sigma}dB(t') \tag{A19}$$

For our system, the state, control and process noise covariance matrices then take the form:

$$F_k = \text{diag}\left(e^{-\gamma^{(1)}\Delta t}, e^{-\gamma^{(2)}\Delta t}, ..., e^{-\gamma^{(N)}\Delta t}\right) \tag{A20}$$

$$G_k = \left(G_k^{(1)}, G_k^{(2)}, ..., G_k^{(N)}\right) \tag{A21}$$

with

$$\begin{aligned} G_k^{(n)} = &f_{\text{em}}^{(n)}(t_1) + \dot{f}_{\text{em}}^{(n)}(t_1)\left[\Delta t + t_k\right] \\ &- e^{-\gamma\Delta t}\left[f_{\text{em}}^{(n)}(t_1) + \dot{f}_{\text{em}}^{(n)}(t_1)t_k\right] \end{aligned} \tag{A22}$$

and

$$Q_k \delta_{kj} = \langle \boldsymbol{\eta}_k \boldsymbol{\eta}_j^\mathsf{T} \rangle = \text{diag}\left(Q^{(1)}, Q^{(2)}, ..., Q^{(N)}\right) \tag{A23}$$

for

$$Q^{(n)} = \frac{-[\sigma^n]^2}{2\gamma^{(n)}}\left(e^{-2\gamma^{(n)}\Delta t} - 1\right) \tag{A24}$$

where Δt is the constant time sampling interval $= t_{k+1} - t_k$.

The remaining component matrices of the Kalman filter that we have not yet specified are the measurement matrix H_k and the measurement covariance matrix R_k. These are defined straightforwardly from Equation (5). Specifically, H_k is a diagonal matrix where the n-th component of the diagonal is given by $g^{(n)}(t_k)$ from Equation (??). The measurement covariance $R_k = E\left[vv^\mathsf{T}\right] = \sigma_{\text{m}}^2$.

APPENDIX B: FIDUCIAL PULSAR VALUES

TK: Do we really need this? The argument is for reproducibility, but we have a nice github repo that holds all the data we actually used, jupyter notebooks that show how the calculations are done. Perhaps it is sufficient to point the reader to the repo...

APPENDIX C: IDENTIFIABILITY

TK TBD. An example calculation for a simple system using the methods of e.g. (Karlsson et al. 2012) (Sedoglavic 2002)

APPENDIX D: WASSERSTEIN DISTANCE

The Wasserstein distance is a metric that defines a distance between two probability distributions $\mu(x)$ and $\nu(x)$. It has an intuitive interpretation as the lowest total cost with which one can move probability mass from μ to ν, with respect to a cost function $c(x, y)$. For this reason it is sometimes known as the "Earth mover's distance". The p-th order Wasserstein distance between two distributions is

$$W_p(\mu, \nu) = \left(\inf_{\gamma \in \Gamma(\mu,\nu)} \int c(x, y)^p d\gamma(x, y)\right)^{1/p} , \tag{D1}$$

where $p \in [1, \infty)$ and $\Gamma(\mu, \nu)$ is the set of all joint probability distributions for (x, y) that have marginals μ and ν, i.e. $\Gamma(\mu, \nu)$ is the set of couplings of μ and ν.

The cost function can be freely chosen for the nature of the problem, but is commonly taken to be the absolute value function, $c(x, y) = |x - y|$, and we adopt the same cost function in this work. Given this choice of $c(x, y)$, for an empirical distribution $\hat{\mu}_n$ composed of n i.i.d samples drawn from the underlying probability distribution μ, the solution to the discrete form of Equation (D3) can be computed generally by the Hungarian algorithm (Kuhn 1955) in polynomial time $O(n^3)$ (Villani 2009). However, for μ defined on $\mathbb{R}^d$ it is well-known (Dudley 1969) that the Wasserstein distance suffers from the curse of dimensionality for dimensions $d \geqslant 3$:

$$E[W_1(\hat{\mu}_n, \mu)] \asymp n^{-\frac{1}{d}} . \tag{D2}$$

In order to circumvent this issue, in this work we calculate the Wasserstein distance exclusively between the one-dimensional marginalized posteriors, i.e. setting $d = 1$. In this case Equation (D3) has a convenient, easily computed, closed form:

$$W_p(\mu, \nu) = \left(\int_0^1 F_\mu^{-1}(z) - F_\nu^{-1}(z)dz\right)^{1/p} \tag{D3}$$

where $F_\mu(z)$ is the cumulative distribution function of μ.

The use of the Wasserstein distance over more common probability measures such as the Kullback–Leibler divergence or the Kolmogorov-Smirnoff test has a number of advantages. Firstly, it is intuitive, being the minimal amount of work required to transform one distribution into another. It also inherits the units of the underlying distributions, providing a convenient heuristic; if $W_1 = 1$ between a pair of distributions with units e.g. radians then we can interpret this as the cost to transform between the two distributions is 1 radian. Further interpretability is provided by the Monge-Kantarovih duality, Equation (??); the difference in the expected value of two random variables drawn from the two distributions is less than 1 radian. Secondly it is a versatile, non-parametric measure that requires no specific properties of the probability distributions that are

being compared such as e.g. Gaussianity. Any two distributions can be compared, irregardless of whether they are continuous, discrete, singular or defined on different metric spaces. Thirdly, it is a true distance metric and as such satisfies desirable properties of a measure of distance such as symmetry and the triangle inequality. It also respects the geometry of the underlying metric space over which the distributions are defined.

REFERENCES

Agazie G., et al., 2023a, ApJ, 951, L8
Agazie G., et al., 2023b, ApJ, 951, L9
Alam M. F., et al., 2021, ApJS, 252, 5
Allen B., 1997, in Marck J.-A., Lasota J.-P., eds, Relativistic Gravitation and Gravitational Radiation. pp 373–417 (arXiv:gr-qc/9604033), doi:10.48550/arXiv.gr-qc/9604033
Antoniadis J., et al., 2023a, arXiv e-prints, p. arXiv:2306.16214
Antoniadis J., et al., 2023b, arXiv e-prints, p. arXiv:2306.16224
Antoniadis J., et al., 2023c, arXiv e-prints, p. arXiv:2306.16226
Arzoumanian Z., et al., 2018, ApJS, 235, 37
Arzoumanian Z., et al., 2020a, ApJ, 900, 102
Arzoumanian Z., et al., 2020b, ApJ, 905, L34
Arzoumanian Z., et al., 2023, arXiv e-prints, p. arXiv:2301.03608
Ashton G., Talbot C., 2021, MNRAS, 507, 2037
Ashton G., et al., 2022, Nature Reviews Methods Primers, 2, 39
Babak S., Sesana A., 2012a, Phys. Rev. D, 85, 044034
Babak S., Sesana A., 2012b, Phys. Rev. D, 85, 044034
Babak S., et al., 2016, MNRAS, 455, 1665
Baym G., Pethick C., Pines D., Ruderman M., 1969, Nature, 224, 872
Bhagwat S., De Luca V., Franciolini G., Pani P., Riotto A., 2021, J. Cosmology Astropart. Phys., 2021, 037
Buchner J., 2021a, arXiv e-prints, p. arXiv:2101.09675
Buchner J., 2021b, The Journal of Open Source Software, 6, 3001
Burke-Spolaor S., et al., 2019, A&ARv, 27, 5
Caballero R. N., et al., 2016, MNRAS, 457, 4421
Charisi M., Taylor S. R., Witt C. A., Runnoe J., 2023, arXiv e-prints, p. arXiv:2304.03786
Chen J.-W., Wang Y., 2022, ApJ, 929, 168
Christensen N., 2019, Reports on Progress in Physics, 82, 016903
Cook S. R., Gelman A., Rubin D. B., 2006, Journal of Computational and Graphical Statistics, 15, 675
Cordes J. M., Lazio T. J. W., 2002, arXiv e-prints, pp astro–ph/0207156
Cordes J. M., Shannon R. M., 2010, arXiv e-prints, p. arXiv:1010.3785
Desvignes G., et al., 2016, Monthly Notices of the Royal Astronomical Society, 458, 3341
Dudley R. M., 1969, The Annals of Mathematical Statistics, 40, 40
Dunbar O. R. A., Duncan A. B., Stuart A. M., Wolfram M.-T., 2022, SIAM Journal on Applied Dynamical Systems, 21, 1539
Dunn L., et al., 2022, MNRAS, 512, 1469
Dunn L., Melatos A., Espinoza C. M., Antonopoulou D., Dodson R., 2023, MNRAS, 522, 5469
Ellis J. A., 2013, Classical and Quantum Gravity, 30, 224004
Ellis J. A., Cornish N. J., 2016, Phys. Rev. D, 93, 084048
Ellis J. A., Siemens X., Creighton J. D. E., 2012, ApJ, 756, 175
Feroz F., Hobson M. P., 2008, MNRAS, 384, 449
Feroz F., Hobson M. P., Bridges M., 2009, Monthly Notices of the Royal Astronomical Society, 398, 1601
Gardiner C., 2009, Stochastic Methods: A Handbook for the Natural and Social Sciences. Springer Series in Synergetics, Springer Berlin Heidelberg, https://books.google.com.au/books?id=otg3PQAACAAJ
Gelb A., Kasper J. F., Nash R. A., Price C. F., Sutherland A. A., eds, 1974, Applied Optimal Estimation. MIT Press, Cambridge, MA
Goldreich P., Julian W. H., 1969, ApJ, 157, 869
Goldstein J. M., Veitch J., Sesana A., Vecchio A., 2018, MNRAS, 477, 5447
Goncharov B., et al., 2021, MNRAS, 502, 478
Gügercinoğlu E., Alpar M. A., 2017, MNRAS, 471, 4827

Handley W. J., Hobson M. P., Lasenby A. N., 2015, MNRAS, 450, L61
Hellings R. W., Downs G. S., 1983, ApJ, 265, L39
Hobbs G. B., Edwards R. T., Manchester R. N., 2006, Monthly Notices of the Royal Astronomical Society, 369, 655
Jaffe A. H., Backer D. C., 2003, The Astrophysical Journal, 583, 616
Jankowski F., et al., 2018, Monthly Notices of the Royal Astronomical Society, 484, 3691
Järvenpää M., Corander J., 2021, arXiv e-prints, p. arXiv:2104.03942
Järvenpää M., Gutmann M., Vehtari A., Marttinen P., 2019, arXiv e-prints, p. arXiv:1905.01252
Jenet F. A., Lommen A., Larson S. L., Wen L., 2004, ApJ, 606, 799
Kalman R. E., 1960, Journal of Basic Engineering, 82, 35
Karlsson J., Anguelova M., Jirstrand M., 2012, IFAC Proceedings Volumes, 45, 941
Kimpson 2023, Geophys. Res. Lett., 50, e2023GL103880
Kuhn H. W., 1955, Naval Research Logistics Quarterly, 2, 83
Lam M. T., et al., 2019, ApJ, 872, 193
Lasky P. D., Melatos A., Ravi V., Hobbs G., 2015, MNRAS, 449, 3293
Lee K. J., Wex N., Kramer M., Stappers B. W., Bassa C. G., Janssen G. H., Karuppusamy R., Smits R., 2011, MNRAS, 414, 3251
Lower M. E., et al., 2021, MNRAS, 508, 3251
Manchester R. N., Hobbs G. B., Teoh A., Hobbs M., 2005, AJ, 129, 1993
McWilliams S. T., Ostriker J. P., Pretorius F., 2014, The Astrophysical Journal, 789, 156
Melatos A., Dunn L. M., Suvorova S., Moran W., Evans R. J., 2020, ApJ, 896, 78
Melatos A., O'Neill N. J., Meyers P. M., O'Leary J., 2023, ApJ, 944, 64
Meyers P. M., Melatos A., O'Neill N. J., 2021a, MNRAS, 502, 3113
Meyers P. M., O'Neill N. J., Melatos A., Evans R. J., 2021b, MNRAS, 506, 3349
Mukherjee P., Parkinson D., Liddle A. R., 2006, ApJ, 638, L51
Pártay L. B., Bartók A. P., Csányi G., 2009, arXiv e-prints, p. arXiv:0906.3544
Parthasarathy A., et al., 2021, MNRAS, 502, 407
Pennucci T. T., Collaboration T. N., 2020, The NANOGrav 12.5-year Wideband Data Set (version 12yv4), doi:10.5281/zenodo.4312887, https://doi.org/10.5281/zenodo.4312887
Perrodin D., Sesana A., 2018, in Rezzolla L., Pizzochero P., Jones D. I., Rea N., Vidaña I., eds, Astrophysics and Space Science Library Vol. 457, Astrophysics and Space Science Library. p. 95 (arXiv:1709.02816), doi:10.1007/978-3-319-97616-7_3
Petiteau A., Babak S., Sesana A., de Araújo M., 2013, Phys. Rev. D, 87, 064036
Pitkin M., 2018, Journal of Open Source Software, 3, 538
Price S., Link B., Shore S. N., Nice D. J., 2012, MNRAS, 426, 2507
Rajagopal M., Romani R. W., 1995, ApJ, 446, 543
Ravi V., Wyithe J. S. B., Shannon R. M., Hobbs G., 2015, MNRAS, 447, 2772
Reardon D. J., et al., 2023, ApJ, 951, L6
Renzini A. I., Goncharov B., Jenkins A. C., Meyers P. M., 2022, Galaxies, 10, 34
Rosado P. A., Sesana A., Gair J., 2015, Monthly Notices of the Royal Astronomical Society, 451, 2417
Sedoglavic A., 2002, Journal of Symbolic Computation, 33, 735
Sesana A., 2013, Classical and Quantum Gravity, 30, 224014
Sesana A., Vecchio A., 2010, Phys. Rev. D, 81, 104008
Sesana A., Vecchio A., Colacino C. N., 2008, Monthly Notices of the Royal Astronomical Society, 390, 192
Shannon R. M., Cordes J. M., 2010a, ApJ, 725, 1607
Shannon R. M., Cordes J. M., 2010b, ApJ, 725, 1607
Simon D., 2006, Optimal State Estimation: Kalman, H Infinity, and Nonlinear Approaches. Wiley-Interscience, USA
Skilling J., 2006, Bayesian Analysis, 1, 833
Sornette D., 2004, Critical phenomena in natural sciences : chaos, fractals selforganization and disorder : concepts and tools
Speagle J. S., 2020, Monthly Notices of the Royal Astronomical Society, 493, 3132
Speri L., Porayko N. K., Falxa M., Chen S., Gair J. R., Sesana A., Taylor S. R., 2023, MNRAS, 518, 1802

Sykes B., Middleton H., Melatos A., Di Matteo T., DeGraf C., Bhowmick A., 2022, MNRAS, 511, 5241

Taylor S. R., Huerta E. A., Gair J. R., McWilliams S. T., 2016, ApJ, 817, 70

Tiburzi C., 2018, Publ. Astron. Soc. Australia, 35, e013

Trassinelli M., 2019, Proceedings, 33

Vargas A., Melatos A., 2023, TBD, 1, 1

Verbiest J. P. W., Weisberg J. M., Chael A. A., Lee K. J., Lorimer D. R., 2012, ApJ, 755, 39

Verbiest J. P. W., Osłowski S., Burke-Spolaor S., 2021, in , Handbook of Gravitational Wave Astronomy. p. 4, doi:10.1007/978-981-15-4702-7_4-1

Villani C., 2009, The Wasserstein distances. Springer Berlin Heidelberg, Berlin, Heidelberg, pp 93–111, doi:10.1007/978-3-540-71050-9_6, https://doi.org/10.1007/978-3-540-71050-9_6

Wan E., Van Der Merwe R., 2000, in Proceedings of the IEEE 2000 Adaptive Systems for Signal Processing, Communications, and Control Symposium (Cat. No.00EX373). pp 153–158, doi:10.1109/ASSPCC.2000.882463

Wyithe J. S. B., Loeb A., 2003, ApJ, 590, 691

Xu H., et al., 2023, Research in Astronomy and Astrophysics, 23, 075024

Yao J. M., Manchester R. N., Wang N., 2017, ApJ, 835, 29

Yardley D. R. B., et al., 2010, MNRAS, 407, 669

Zarchan P., Musoff H., 2000, Fundamentals of Kalman Filtering: A Practical Approach. Progress in astronautics and aeronautics, American Institute of Aeronautics and Astronautics, https://books.google.com.au/books?id=AQxRAAAAMAAJ

Zhu X. J., et al., 2014, MNRAS, 444, 3709

Zhu X.-J., et al., 2015a, Monthly Notices of the Royal Astronomical Society, 449, 1650

Zhu X.-J., et al., 2015b, Monthly Notices of the Royal Astronomical Society, 449, 1650

Zhu X.-J., Wen L., Xiong J., Xu Y., Wang Y., Mohanty S. D., Hobbs G., Manchester R. N., 2016, Monthly Notices of the Royal Astronomical Society, 461, 1317

Zic A., et al., 2023, arXiv e-prints, p. arXiv:2306.16230

van Eysden C. A., Melatos A., 2010, MNRAS, 409, 1253

This paper has been typeset from a TEX/LATEX file prepared by the author.